Dissertation

Application of NEMS-FTIR for Micro- and Nanoplastic Detection in Water: A Study on Artificially Weathered Polymer Samples

ausgeführt zum Zwecke der Erlangung des akademischen Grades einer Diplom-Ingenieurin, eingereicht am

Institut für Sensor- und Aktuatorsysteme
Technische Universität Wien

vorgelegt von:
Eldira Sesto B.Sc.
Matrikelnummer: 11815163

Wien, am May 26, 2025

betreut von:
Univ. Prof. Dr. Silvan Schmid
Jelena Timarac-Popovic M.Sc.

Eidesstattliche Erklärung

Ich erkläre an Eides statt, dass ich die vorliegende Masterarbeit selbstständig und ohne fremde Hilfe verfasst, andere als die angegebenen Quellen und Hilfsmittel nicht benutzt bzw. die wörtlich oder sinngemäß entnommenen Stellen als solche kenntlich gemacht habe.

Wien, May 26, 2025

Unterschrift (Author)

Nothing in life is to be feared, it is only to be understood. Now is the time to understand more, so that we may fear less.
- Marie Curie

Contents

Abstract

Nanoplastics have become an increasing environmental concern due to their ability to spread easily, remain in ecosystems for long periods, and potentially affect human health. Traditional detection methods like FTIR and Raman spectroscopy often struggle to detect such small particles because of their limited resolution and sensitivity. This thesis investigates the use of nanoelectromechanical systems-based Fourier-transform infrared spectroscopy (NEMS–FTIR) to detect and analyze nanoplastics in water. The study focused on how polyamide (PA) and polystyrene (PS) materials break down under artificial weathering over 25 days. Polyethylene terephthalate (PET) was also considered initially but later excluded because it showed minimal changes during the experiment.

Plastic samples, including teabags, bottle pieces, lids, and particles, were exposed to cycles of UV light and temperature changes that simulated one year of natural weathering. A nebulizer was used to evenly apply the samples onto NEMS chips. NEMS–FTIR spectra were recorded and analyzed using a Python-based workflow that enabled normalization, background subtraction, and identification of key vibrational features. The results showed chemical changes over time, such as stronger O–H/N–H signals and oxidation-related modifications in PA and PS samples.

This study confirms the high sensitivity and selectivity of NEMS–FTIR for early-stage nanoplastic detection, highlighting its potential for real-world environmental monitoring and as a complementary tool to existing analytical techniques.

Kurzfassung

Nanoplastik stellt ein wachsendes Umweltproblem dar, da es sich leicht verbreiten kann, lange in Ökosystemen verbleibt und potenziell Auswirkungen auf die menschliche Gesundheit hat. Herkömmliche Nachweismethoden wie FTIR- und Raman-Spektroskopie stoßen beim Nachweis so kleiner Partikel aufgrund begrenzter Auflösung und Empfindlichkeit an ihre Grenzen. In dieser Arbeit wird der Einsatz von nanoelektromechanischen Systemen kombiniert mit Fourier-Transform-Infrarotspektroskopie (NEMS–FTIR) zur Detektion und chemischen Analyse von Nanoplastik in Wasser untersucht. Der Fokus liegt auf dem Abbauverhalten von Polyamid (PA) und Polystyrol (PS) unter künstlicher Verwitterung über einen Zeitraum von 25 Tagen. Polyethylenterephthalat (PET) wurde zunächst berücksichtigt, aber aufgrund geringer Veränderung im Experiment nicht weiter analysiert.

Die Kunststoffproben – darunter Teebeutel, Flaschenstücke, Deckel und Partikel – wurden UV-Licht- und Temperaturzyklen ausgesetzt, die ein Jahr natürlicher Verwitterung simulierten. Für die gleichmäßige Probenauftragung auf die NEMS-Chips wurde ein Vernebler verwendet. Die NEMS–FTIR-Spektren wurden aufgenommen und mit einem Python-basierten Workflow analysiert, der Normalisierung, Hintergrundsubtraktion und die Identifikation wichtiger Schwingungsbanden ermöglichte. Die Ergebnisse zeigten chemische Veränderungen im Zeitverlauf, darunter verstärkte O–H/N–H-Signale und oxidationsbedingte Modifikationen in PA- und PS-Proben.

Diese Studie bestätigt die hohe Empfindlichkeit und Selektivität von NEMS–FTIR zur frühzeitigen Erkennung von Nanoplastikabbau und unterstreicht das Potenzial der Methode für den realitätsnahen Umweltnachweis sowie als Ergänzung zu bestehenden analytischen Verfahren.

Acknowledgment

I would like to sincerely thank Univ. Prof. Dr. Silvan Schmid for the opportunity to conduct my thesis within his research group and for the valuable input and guidance throughout the process. His support provided an important framework for the development of this work.

I also wish to thank my co-supervisor, Jelena Timarac-Popovic, M.Sc., for her continuous support, countless helpful discussions, and patience. Her detailed feedback and encouragement were incredibly valuable, both scientifically and personally.

I am deeply grateful to my family for always putting my education and goals first, and for their constant support throughout my studies. I especially thank my mother, whose strength, love, and prayers carried me through every challenge. I dedicate this work to the memory of my beloved father, who inspired my love for education, books, and science. Even though he did not live to see my success, his love and belief in me still guide everything I do.

I'm also thankful to my partner — my biggest supporter, who believed in me even when I didn't, helped me in every way he could, and was always there to calm me down when things didn't go as planned.

To my colleagues and friends: thank you for standing by me, sharing ideas, and helping me stay motivated during the difficult moments of this journey.

Chapter 1

Fundamentals

1.1 Introduction to Nanoplastics

Nanoplastics are an increasingly concerning environmental and health issue, due to their small size, persistence, and potential to accumulate in organisms and ecosystems. These plastic particles fall within the nanometer range, though their exact size definition remains debated. Some authors define nanoplastics as particles smaller than 1000 nm (1 µm), which aligns with broader classifications of nano-sized materials [1]. Others adopt a more restrictive definition of less than 100 nm, in line with the general definition of engineered nanomaterials [2–5]. Most scientific publications explicitly state the threshold they use, reflecting the lack of consensus in the field. Beyond size, nanoplastics are also characterized by their origin, typically as degradation products of larger plastics resulting from environmental processes such as weathering, mechanical abrasion, and chemical decomposition [6]. These definitions emphasize both their small scale and the diverse pathways through which they enter ecosystems.

Nowadays, nanoplastics are widespread in the environment due to their diverse sources. They can originate from the fragmentation of larger plastic waste, the inclusion of microbeads in personal care products, wear and tear of synthetic textiles, and the abrasion of tires. Industrial discharges and wastewater treatment plants further worsen their spread, as these facilities often lack the capability to effectively capture such small particles [7]. Additionally, manufacturing processes for nanoplastics and other industrial applications, such as paints and coatings, are direct sources of their release into the environment [8].

The detection of nanoplastics across a wide range of environments highlights their widespread presence. They have been identified in marine ecosystems, freshwater bodies, soil, and even atmospheric particles [9]. Once released, they are readily transported via wind, water currents, and biota, allowing them to spread over long distances. Their persistence and mobility raise concerns about their long-term ecological impacts, particularly in ecosystems where they accumulate over time [10].

Nanoplastics also pose risks to food safety and human health. Studies have confirmed their presence in seafood, such as fish and shellfish, as well as in common products like table salt, honey, and bottled water [11]. This widespread presence indicates that consuming contaminated food and water may be one of the primary ways humans are exposed to nanoplastics. Furthermore, they have been detected in consumer products such as cosmetics and industrial paints, creating additional pathways for human contact [12]. Recent investigations have revealed nanoplastics in human tissues, including blood, the placenta, lungs, and even the brain, underscoring their ability to penetrate biological barriers and accumulate in sensitive areas [13, 14].

In addition to their physical presence, nanoplastics carry chemical and biological risks. Their large surface-to-volume ratio enables them to adsorb toxic substances, such as heavy metals and persistent organic pollutants, which can then be transported into organisms that ingest them [11]. The creation of "plastispheres" on their surfaces—a microbial community that thrives on plastics—further complicates their impact, as these communities can harbor pathogenic microorganisms and facilitate the spread of antibiotic resistance [15].

Despite growing evidence of their environmental and health impacts, regulatory frameworks addressing nanoplastics remain underdeveloped. Most policies focus on microplastics, leaving nanoplastics less regulated despite their unique hazards. Current legislation does not adequately consider the specific pathways of nanoplastic exposure, such as their presence in drinking water and their ability to penetrate living tissues [16]. Policymakers face challenges in establishing standardized definitions and methods for quantifying nanoplastics, which are crucial for effective regulation and mitigation strategies [17].

Detecting nanoplastics presents numerous challenges due to their size, low environmental concentrations, and chemical diversity. Common analytical techniques such as Fourier transform infrared spectroscopy (FTIR) and Raman spectroscopy are widely used for the chemical identification of plastic particles, but often face limitations such as low throughput, complex sample preparation, or spectral interferences [18–20]. More advanced methods, such as pyrolysis-gas chromatography-mass spectrometry (Py-GC/MS), can detect nanoplastics in complex matrices but are time-consuming and require costly instrumentation [21, 22].

These limitations have motivated the exploration of alternative detection techniques, including nanoelectromechanical systems, which are discussed in the following sections.

Recently, nanoelectromechanical IR spectroscopy (NEMS-IR) has emerged as a promising alternative, offering high chemical specificity, broad spectral coverage, and minimal sample requirements. The photothermal mechanism behind NEMS sensing enables chemical identification through frequency shifts in a nanomechanical membrane resonator [23]. Furthermore, its compatibility with in-situ thermal desorption allows for the separation of analyte mixtures prior to detection, enhancing its utility in analyzing complex synthetic samples [24]. These capabilities make NEMS-IR a valuable addition to the growing set of tools for nanoplastic detection.

Understanding the multifaceted impacts of nanoplastics is essential for addressing their environmental and health implications. By integrating insights from recent research, this introduction provides a foundational overview, highlighting the need for innovative detection methods, comprehensive regulations, and sustainable practices to mitigate the risks associated with nanoplastics.

Research Goals

The aim of this thesis is to investigate the chemical and structural degradation of selected plastic materials under artificially induced weathering conditions. A key objective is to assess whether nanoelectromechanical system-based Fourier-transform infrared spectroscopy (NEMS–FTIR) can serve as a sensitive and reliable method for detecting nanoplastics in aqueous samples at early stages of degradation.

To achieve this, the following goals were defined:

- To simulate environmental weathering through a 25-day accelerated UV and thermal exposure protocol.
- To monitor macroscopic changes and mass variation in PS, PA, and PET samples.
- To track the evolution of specific vibrational bands associated with degradation, such as O–H/N–H, amide I and II, and C–H stretching regions, using NEMS–FTIR.
- To assess the suitability of NEMS–FTIR for detecting chemical changes in plastic degradation products without sample pre-concentration or filtration.

1.2 Plastics Used in the Study

In this study, three widely used polymers have been examined: polystyrene (PS), polyethylene terephthalate (PET), and polyamide (PA), specifically nylon 6. These specific polymers have been chosen due to their unique structural properties, presence in the environment, and different degradation rates, allowing an in-depth analysis of plastic breakdown processes caused by accelerated weathering conditions.

Polystyrene (PS)

PS is one of the most important modern plastic industry materials and has been used worldwide because of its low cost and outstanding physical properties [25]. However, PS is also particularly vulnerable to photodegradation when exposed to ultraviolet (UV) radiation, which represents some remarkable environmental challenges [26].

The PS chemical structure consists of benzene rings attached to a linear hydrocarbon backbone, which contribute to its stability and rigidity. Despite that, this particular structure also makes the material vulnerable to degradation influenced by UV radiation. As described by Yousif and Haddad [27], the primary initializer of PS degradation is the photooxidative process.

Under UV light, PS undergoes chain scission, where free hydrogen radicals are formed, which are mobilized within the polymer matrix. The free radicals can then abstract hydrogen atoms from nearby polymer chains, which leads to further breakage of bonds and the creation of additional free radicals. This degradation process leads to a loss in molecular weight, embrittlement, and change of color (yellowing) [27–29].

While the benzene rings offer some resistance to chemical breakdown, they also absorb UV light and contribute to the photodegradation of PS. During UV exposure, less labile phenyl radicals in the structure also interact with light to further promote degradation. The resultant oxidative damage with chronic exposure becomes significant and manifests as surface cracking, brittleness, and breakdown into smaller particles, such as micro- and nanoplastics [28, 29]. Figure 1.1 shows the chemical structure of PS. This leads to the conclusion that PS is stable against mild environmental conditions and can thus be used for extended periods.

For this study, PS was chosen because of its wide use among different industries and its significant impact on plastic pollution around the world. It represents one of the major concerns for the environment, as it is one of the 6 most consumed and produced polymers,

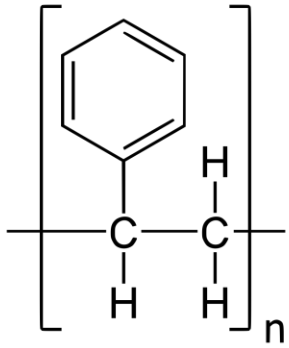

Figure 1.1: The Chemical Structure of Polystyrene [30]

and is found abundantly in the sea [31–33]. In the accelerated weathering experiment, PS was expected to degrade at a moderate pace, due to its structure and UV sensibility.

Polyamide (PA, Nylon 6)

PA, also commonly referred to as nylon, is another crucial material in modern-day industry, known for its good mechanical properties, versatility, and resilience. Particularly, nylon 6 is commonly used because of its thermal resistance, chemical stability, and high strength, which makes it usable in a wide range of applications, such as textile, packaging, and different engineering components [34]. On the other hand, the materials' durability proved to be a great environmental challenge, especially when the material enters waste streams and aquatic environments [35].

Like other nylons, nylon 6 is a polyamide, which means it has repeating amide linkages on its backbone. These linkages are responsible for the bonding of hydrogen between polymer chains, which improves materials' strength and stiffness. This bonding results in a semi-crystalline structure, which contributes to durability and makes the material resistant to mild environmental conditions [36]. Figure 1.2 shows the chemical structure of Nylon 6.

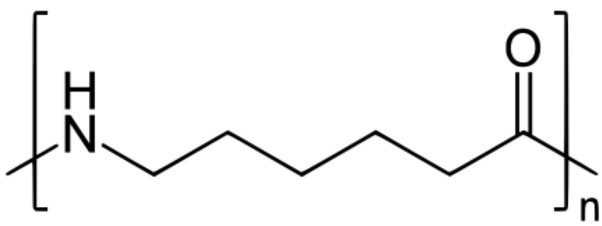

Figure 1.2: The Chemical Structure of Nylon 6 [37]

Nylon 6 was chosen for this study since it is used widely in industry and textile production as well for its environmental durability. It is considered to be among the most common synthetic fibers in environmental samples, especially in microplastic form [35].

In the accelerated weathering experiment, PA (nylon 6) was expected to start degrading at a slower pace, compared to other plastics, including PS, considering its crystalline structure and strong hydrogen bonding of molecules.

Polyethylene Terephthalate (PET)

For years, PET has been one of the most used thermoplastic polymers and is particularly known for its transparency, strength, and chemical durability. The mentioned properties are what make PET a great choice for the manufacture of bottles, food containers, and different kinds of packaging. Global production of PET reached 41 million tonnes in 2014 and is expected to keep growing [38].

Even though PET bottles are recycled efficiently, a great proportion escapes from waste management systems and ends up in the oceans [39].

PET chemical structure is made of repeating ester bonds (-COO-) within a semi-crystalline matrix. The fact that each monomer unit has a benzene ring leads to the materials' chemical stability and makes it applicable in mild environmental conditions [40]. Even though PET is resistant to many forms of chemical degradation, it remains vulnerable to photooxidative degradation when exposed to UV light. Figure 1.3 shows the chemical structure of PET.

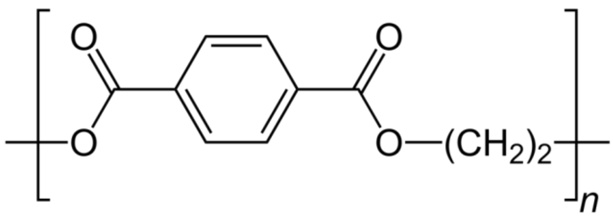

Figure 1.3: The Chemical Structure of PET [41]

For this study, PET was selected due to its widespread use and the fact that it is considered one of the main environmental pollutants, especially in microplastic form.

Regarding the accelerated weathering experiment, PET was expected to degrade at a slower rate than plastic types like PS. Including PET in this study allowed us to investigate a wider range of degradation behaviors, including both materials that degrade easily and materials that take longer periods for degradation. The diversity helps obtain a more comprehensive view and gain a better understanding of how different polymer structures influence degradation rates and environmental pollution in micro- and nanoplastic form.

1.3 Accelerated Weathering Process

Accelerated weathering is a time-compressed laboratory simulation of the environmental degradation of materials through exposure to controlled cycles of UV light, heat, and humidity [42]. This methodology is particularly useful in the studies of long-term durability and breakdown pathways of polymers, such as PE, PP, and PS, as it allows researchers to simulate years of environmental exposure within weeks or months [43]. Accelerated weathering helps show the environmental impacts on plastics and their interactions within ecosystems by understanding how these materials degrade into micro- and nanoplastics under simulated conditions.

Several studies have shown that UV light is the most important factor when it comes to degradation. Exposure to UV radiation initiates photochemical reactions that weaken polymer structures, leading to molecular scission and surface oxidation. For instance, research on PS subjected to high-intensity UV light demonstrated extensive surface oxidation and crack formation, which facilitated the release of micro- and nanoplastics, highlighting how such degradation products may persist in natural environments [42–45].

Experimental setups for accelerated weathering vary widely but typically involve specialized chambers like QUV and Q-SUN, which use xenon arc or UV-A/UV-B fluorescent lamps to simulate sunlight exposure at intensities that can reach up to five times that of natural sunlight. For example, a study on low-density polyethylene (LDPE) used a QUV chamber to expose samples to high levels of UV-A radiation, resulting in significant oxidation, embrittlement, and fragmentation within a few weeks. Under natural sunlight, such degradation might take years, making accelerated weathering invaluable for understanding the rate and characteristics of polymer breakdown [46]. High temperatures and humidity cycles are often incorporated to replicate environmental conditions more realistically, simulating fluctuations found in outdoor settings. Polypropylene (PP) and PET exposed to a combination of UV radiation and elevated temperatures (up to 60°C) showed rapid molecular breakdown, characterized by increased surface roughness and brittleness due to oxidation. By adjusting singular factors like UV intensity, temperature, and humidity, researchers can more accurately simulate diverse real-world environments, from sunny shorelines to urban landscapes [47, 48].

To ensure consistency and comparability in accelerated weathering studies, several standards define the specific cycles, light sources, and temperature and humidity settings to be used in testing. ASTM D4329 [49] and ISO 4892-3 [50] are commonly referenced standards for exposing plastics to UV light and moisture using fluorescent UV lamps, often specifying cycles like 8 hours of UV exposure at 60°C followed by 4 hours of condensation or darkness at a lower temperature, simulating day and night conditions. ASTM G154 [51] and ISO 4892-2 [52] are frequently applied when testing plastics with fluorescent and xenon arc lamps, respectively, as they cover exposure cycles that mimic full-spectrum sunlight and alternating moisture conditions. In setups focused on simulating outdoor conditions more precisely, ASTM G155 [53] also provides guidance for xenon arc exposure with intermittent water spray cycles, which help simulate effects like rain or dew. These standards are widely adopted in the materials testing industry, guiding the design of accelerated weathering tests to ensure consistent results and accurate simulation of natural degradation [46].

In recent years, innovative low-cost setups have also been developed to make accelerated weathering more accessible. One such system, detailed in [54], includes UV light exposure and temperature control alongside mechanical agitation to simulate marine conditions. This system replicates oceanic environments at a fraction of the cost of traditional weathering chambers by combining UV lamps and constant agitation to induce photooxidative and mechanical degradation. This approach effectively demonstrated surface oxidation and particle fragmentation in materials such as PS and PET under simulated marine conditions, validating its effectiveness in providing environmentally relevant results [48].

The primary mechanisms behind accelerated weathering are photodegradation, oxidative degradation, and thermal degradation. Photodegradation occurs when UV light interacts with polymers, breaking chemical bonds and forming reactive radicals that degrade the material. Studies on polystyrene exposed to xenon arc lamps have shown this process at work, with the surface gradually developing cracks and roughness that lead to particle formation as degradation progresses [44, 55]. Thermal degradation often complements photodegradation, as high temperatures can further destabilize polymer structures. This effect is particularly pronounced in semi-crystalline polymers such as LDPE, where elevated temperatures promote oxidative reactions and increase crystallinity, resulting in brittleness and subsequent fragmentation. Researchers found that when LDPE samples were exposed to combined high temperatures and UV light, the molecular structure weakened considerably, leading to the release of microplastic fragments like those that might be found in real-world environments such as beaches [39, 46].

The environmental implications of accelerated weathering studies are significant, as the research demonstrates that weathered plastics produce micro- and nanoplastics with enhanced surface reactivity, which increases their capacity to adsorb pollutants and interact with biological organisms. For instance, accelerated weathering studies on LDPE have shown that the surface of these plastics becomes more hydrophilic after extended UV exposure, increasing the likelihood of adsorbing environmental contaminants if found in aquatic environments [56]. Furthermore, insights from accelerated weathering inform the design of more resilient polymers, as researchers can use these findings to develop additives and stabilizers that extend polymer durability under environmental stress. This approach also guides the creation of eco-friendly plastics with reduced environmental impact, offering a pathway toward minimizing pollution by developing materials that better withstand degradation [48, 57].

To summarize, accelerated weathering provides a controlled, efficient means of understanding plastic degradation and its ecological impact. The insights gained from these studies play a crucial role in advancing both environmental science and material innovation, as they help predict the environmental fate of polymers and guide sustainable design practices that address the pressing issue of plastic pollution.

1.4 NEMS Resonator

Nanoelectromechanical systems (NEMS), commonly referred to as NEMS resonators or NEMS chips, are highly sensitive mechanical devices engineered to oscillate at their natural frequencies. These frequencies, known as eigenfrequencies, are determined by the resonator's inherent physical properties, such as its mass, stiffness, geometry, and material composition. The principle of mechanical resonance underpins their operation. When a NEMS resonator is driven at its resonant frequency, the amplitude of its oscillation is maximized, allowing it to detect even slight physical changes in its environment. This phenomenon makes NEMS resonators exceptionally useful in sensing applications, where detecting small variations is paramount [58].

As defined by Schmid et al. [59], a resonator is "a mechanical system that vibrates at one or more of its natural frequencies, which are determined by its physical properties such as mass, stiffness, and geometry." This fundamental definition highlights the interplay of mechanical properties that make these devices sensitive to external influences, such as mass changes or temperature variations. The ability to translate these interactions into measurable shifts in resonant frequency forms the foundation of their application in advanced sensing technologies. The unique characteristics of NEMS resonators arise from their nanoscale dimensions, which allow them to achieve higher sensitivity compared to microscale or macroscale counterparts. Their small mass and high resonant frequencies, typically in the MHz to low GHz range [60,61], amplify the effects of external perturbations, making them particularly effective for detecting trace-level interactions, such as the adhesion of nanoplastics or other nanoparticles. Additionally, their compact size enables integration into portable systems, further enhancing their applicability in environmental monitoring, medical diagnostics, and materials research [62].

1.4.1 Modes of Oscillation

In NEMS resonators, modes of oscillation refer to the specific patterns in which the system vibrates. Each mode is characterized by a unique natural frequency (eigenfrequency), which depends on the resonator's material properties, geometry, and external conditions. These modes are central to the resonator's functionality, as they define how the device interacts with external stimuli such as added mass, thermal effects, or mechanical forces. In practical terms, a mode of oscillation is described by the number of nodes and antinodes formed during vibration. Nodes are points of zero displacement, while antinodes are points of maximum displacement. These spatial configurations enable the resonator to produce distinct responses under varying excitation conditions, making them versatile for applications in sensing and signal processing. The eigenfrequencies of a NEMS resonator are mathematically derived from the two-dimensional wave equation, which governs the behavior of elastic membranes.

As defined in [59], the governing equation for the vibration of a membrane is given by:

$$\sigma \nabla^2 u - \rho \frac{\partial^2 u}{\partial t^2} = 0 \tag{1.1}$$

where:

- σ is the tensile stress,
- ρ is the density of the material,
- u represents the displacement of the membrane at a given time and position.

For a rectangular membrane, the eigenfrequencies ($\omega_{n,j}$) are given by:

$$\omega_{n,j} = \sqrt{\frac{\sigma}{\rho}}\sqrt{\frac{n^2\pi^2}{L_x^2} + \frac{j^2\pi^2}{L_y^2}} \tag{1.2}$$

where:

- L_x and L_y are the membrane's dimensions,
- n and j are the mode indices indicating the number of nodes along the x and y directions, respectively.

These modes define the spatial distribution of vibrations on the membrane, with higher mode indices corresponding to more complex vibration patterns.

Physical Interpretation and Practical Relevance

When it comes to physical interpretation and practical relevance, each mode of oscillation represents a specific way the resonator vibrates under excitation. For example:

- The fundamental mode (where n = 1, j = 1) is the simplest pattern, with one antinode at the center and no internal nodal lines.
- Higher-order modes (e.g., n = 2, j = 1; n = 1, j = 2; or n = 2, j = 2) feature multiple nodes and antinodes. While these modes often have lower amplitudes, they can provide enhanced sensitivity to localized perturbations, such as small particles interacting with specific regions of the resonator.

As shown in Figure 1.4, the vibrational modes of a square membrane illustrate the progression from the fundamental mode to higher-order modes. The (1,1) mode, being the simplest, has no internal nodes, while the (2,2) mode demonstrates the increasing complexity of oscillation patterns with additional nodal lines dividing the membrane into distinct oscillation regions.

In sensing applications, tracking these modes provides a deeper understanding of how external factors, such as mass, influence the resonator's behavior. Higher modes may also reveal spatial information about where mass or energy is distributed on the membrane.

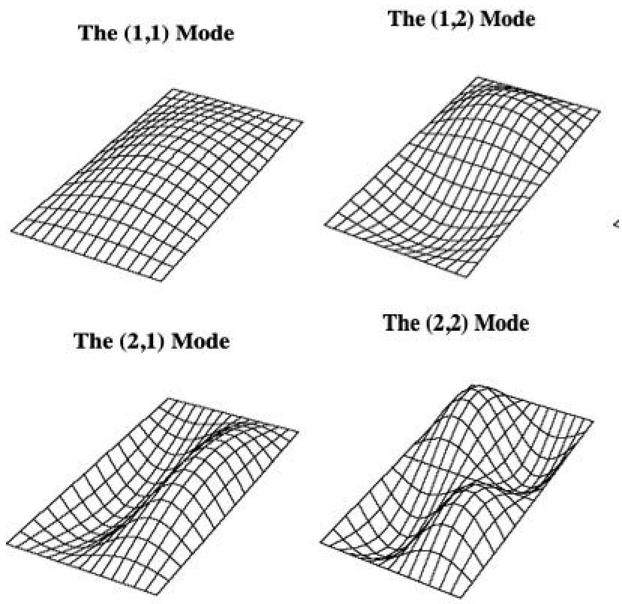

Figure 1.4: Vibrational modes of a square membrane, including the fundamental mode (1,1) and higher-order modes (1,2), (2,1), and (2,2). These modes demonstrate the increasing complexity of oscillation patterns. Source [63]

Modes of Oscillation in Photothermal Detection

In the context of photothermal detection, modes of oscillation play a critical role in enhancing the sensitivity and accuracy of NEMS resonators. When deposited particles absorb IR light, the resulting photothermal heating causes localized expansion and modifies the resonator's tension. This, in turn, shifts the resonant frequency in specific modes. By analyzing these shifts, the system can quantify the thermal and mechanical effects caused by the particles, providing insights into their size, composition, and thermal properties.

The study by Chien [64] demonstrates how multi-mode analysis is used to improve detection precision. By tracking higher-order modes alongside the fundamental mode, the detection system can achieve a more nuanced response, enabling the differentiation of particles with similar properties.

Advantages of Multi-Mode Analysis

Using multiple modes of oscillation has several advantages:

- Enhanced sensitivity: Higher modes are more sensitive to localized changes, allowing for the detection of smaller or distributed masses.

- Spatial resolution: Different modes provide spatially distinct vibration patterns, which can help determine the location of interactions on the resonator surface.

- Noise reduction: Monitoring multiple modes helps differentiate true signals from noise, improving the overall reliability of measurements.

1.4.2 Resonant Frequency and Frequency Shifts

The resonant frequency (f_0) of a NEMS resonator is a fundamental property that defines the natural oscillation rate of the system. At this frequency, the resonator vibrates most efficiently, with maximum energy exchange between kinetic and potential forms. This characteristic makes the resonant frequency a critical parameter for applications requiring precise detection, such as identifying mass changes, thermal effects, or mechanical perturbations at the nanoscale [60].

The resonant frequency is determined by the system's mechanical properties, including its stiffness (k) and effective mass (m). Mathematically, it is expressed as:

$$f_0 = \frac{1}{2\pi}\sqrt{\frac{k}{m}} \tag{1.3}$$

where:

- k represents the stiffness or spring constant of the resonator, reflecting its resistance to deformation,

- m is the effective mass of the resonating structure.

The formula illustrates that an increase in stiffness raises the resonant frequency, while an increase in mass lowers it. This relationship underpins the resonator's ability to detect external influences, as any alteration in mass or stiffness will directly shift the frequency.

1.4.3 Frequency Shifts Due to Mass Changes

When an external mass (Δm) interacts with the resonator, such as through particle adhesion or deposition, the system's total mass increases, resulting in a measurable frequency shift. According to [58] the new frequency (f_{new}) can be approximated as:

$$f_{new} = f_0 \cdot \sqrt{\frac{m}{m + \Delta m}} \tag{1.4}$$

where:

- f_{new} is the new eigenfrequency after mass (Δm) is added.
- f_0 is the original eigenfrequency of the resonator.
- m is the effective mass of the resonator before the mass change.
- Δm is the added mass to the resonator.

This equation illustrates that the addition of mass (Δm) decreases the resonator's eigenfrequency (f_{new}). Such behavior is foundational in mass-sensing applications, where frequency shifts provide insight into the added or removed mass at the nanoscale.

1.4.4 Approximation for Small Added Mass

For cases where the added mass (Δm) is much smaller than the resonator's mass (m), the formula can be approximated to simplify calculations [65]. Using the equation 1.4 we rewrite the denominator as:

$$\frac{m}{m + \Delta m} = \frac{1}{1 + \frac{\Delta m}{m}}.$$

Using a Taylor series expansion for small values of $\frac{\Delta m}{m}$, we approximate:

$$\sqrt{\frac{1}{1 + \frac{\Delta m}{m}}} \approx 1 - \frac{\Delta m}{2m}.$$

Substituting this into the eigenfrequency equation:

$$f_{\text{new}} \approx f_0 \left(1 - \frac{\Delta m}{2m}\right).$$

The frequency shift Δf is given by:

$$\Delta f = f_{\text{new}} - f_0,$$

so:

$$\Delta f \approx -\frac{f_0}{2m} \Delta m.$$

Here, m is often denoted as m_0 (the resonator's original mass), leading to:

$$\Delta f \approx -\frac{f_0}{2m_0} \Delta m.$$

This approximation is widely used for resonators in sensing applications, as it simplifies the analysis while maintaining accuracy for small Δm.

The relationship between mass and frequency shift forms the foundation of mass sensing using nanomechanical resonators. When nanoplastics adhere to the resonator, even tiny added masses induce measurable frequency changes, enabling real-time and non-invasive detection in environmental applications.

1.5 Actuation and Tracking of Resonant Frequencies

The ability to excite nanomechanical resonators and detect their oscillation lies at the core of their application in sensing. This process, known as transduction, involves converting electrical or optical energy into mechanical motion (actuation), and conversely, converting mechanical motion into a measurable electrical or optical signal (readout). Several distinct mechanisms have been developed to achieve this, each offering specific advantages depending on integration compatibility, sensitivity, and experimental conditions.

1.5.1 Electrodynamic Transduction

Electrodynamic transduction is based on the Lorentz force that arises when a current-carrying conductor is placed in a static magnetic field. In this setup, an alternating current is passed through a metallic layer on the resonator, which is positioned in a uniform magnetic field. The interaction between the current and magnetic field generates a Lorentz force that excites mechanical vibration in the structure. Simultaneously, the motion of the resonator within the magnetic field induces an electromotive force (EMF) that can be measured as a voltage across the conductor. In nanomechanical systems, electrodynamic transduction is most commonly implemented in this form, known as magnetomotive transduction. This approach enables both actuation and readout using the same principle and is widely used in high-frequency NEMS due to its simplicity and robustness [59]. It enables efficient operation at frequencies reaching into the gigahertz range, and was a foundational technique in some of the earliest experimental demonstrations of nanomechanical resonators [66]. However, it requires an external magnetic field and may introduce magnetomotive damping, which can reduce the resonator's quality factor [67, 68].

1.5.2 Electrostatic Transduction

Electrostatic transduction relies on the interaction between quasi-static electric charges and is one of the most commonly used actuation and readout methods in MEMS and NEMS devices. It operates by applying a voltage between a resonator and a nearby electrode, generating an attractive electrostatic force that induces mechanical motion. The displacement modifies the capacitance between the electrodes, and this variation can be detected as a change in current or voltage, enabling precise readout. Electrostatic transduction allows for low-power operation and is highly compatible with CMOS processes, making it ideal for system integration and miniaturization. It has been successfully employed in a variety of MEMS devices, including accelerometers, gyroscopes, microphones, and micromirror arrays [59]. In nanomechanical resonators, however, the reduced size of the moving structures leads to significantly smaller electrostatic signals, posing a challenge to sensitivity. Additionally, locally trapped charges, such as those at dielectric interfaces, can interfere with effective actuation and detection and must be carefully considered in transducer design [69].

1.5.3 Piezoelectric and Piezoresistive Transduction

Both piezoresistive and piezoelectric transduction rely on the coupling between mechanical strain and electrical signals, enabling their use for displacement detection, and in the case of piezoelectric materials, for actuation as well. These methods are particularly useful in nanomechanical systems where electrical readout is desired and optical access may be limited [59].

In piezoresistive transduction, the electrical resistance of a strain-sensitive element changes as the resonator undergoes mechanical deformation. This resistance change is measured and related to the displacement of the structure. The sensitivity of the transduction is characterized by the gauge factor, which depends on both geometric deformation and the intrinsic properties of the material. In practice, piezoresistive sensing elements are often implemented using metal or semiconductor thin films configured in Wheatstone bridges or downmixing circuits [70, 71]. While semiconductors offer high gauge factors, metals such as gold are frequently preferred in NEMS due to their low impedance and low electrical noise. Although gold exhibits a lower gauge factor, its low resistance simplifies readout circuitry and enables high-frequency detection without significant signal amplification [72].

Piezoelectric transduction, in contrast, utilizes materials that generate an electric charge when mechanically deformed and conversely exhibit strain when subjected to an external electric field. This bidirectional electromechanical coupling allows the same layer to serve for both actuation and sensing. Actuation is typically achieved by applying an electric field across a piezoelectric layer deposited asymmetrically with respect to the resonator's neutral axis, which results in a bending moment that drives vibration. During detection, the mechanical motion of the resonator induces a time-varying electric displacement field in the piezoelectric material, which produces a measurable current. The effectiveness of this transduction depends on the piezoelectric material properties, especially the piezoelectric coefficients [59]. Among available materials, aluminum nitride has become a preferred choice for piezoelectric NEMS due to its strong electromechanical coupling, compatibility with standard CMOS fabrication processes, and the ability to be deposited in thin, c-axis-oriented films. This enables the fabrication of nanoscale piezoelectric devices with excellent integration potential [73,74]. Together, piezoresistive and piezoelectric transduction methods offer complementary strengths: piezoresistive elements are simpler and easier to integrate for readout, while piezoelectric layers enable simultaneous actuation and sensing with high signal fidelity in compact device architectures.

1.5.4 Optical Actuation and Detection

Optical techniques offer powerful and contact-free means of actuating and detecting nanomechanical motion, and are widely used in both experimental setups and integrated systems. Optical transduction can be categorized into external (off-chip) and integrated (on-chip) methods. External techniques, such as interferometry, laser-Doppler vibrometry, and optical leverage, require only optical access to the resonator and are often used for rapid characterization of prototypes. In contrast, integrated optical methods, such as Mach–Zehnder interferometers, evanescent coupling, and waveguide-based detection, enable miniaturized and scalable solutions that overcome the diffraction limit and eliminate the need for precise laser alignment [59].

Interferometric detection, including configurations like Fabry–Pérot, Michelson, and Mach–Zehnder interferometers, allows extremely precise measurement of displacement by detecting phase shifts in a light wave caused by the resonator's motion [75–77]. These methods are typically limited by the need for phase stability and coherent light sources. In contrast, laser-Doppler vibrometry (LDV) detects velocity rather than displacement by measuring the Doppler shift in a laser beam reflected from a vibrating surface [59]. LDV systems are commercially available with gigahertz bandwidths and do not require phase stabilization, making them ideal for high-speed measurements.

Other readout mechanisms include optical leverage, which measures the angular deflection of a beam using a position-sensitive detector, and end-coupled waveguide detection, where the vibrating resonator modulates optical coupling between waveguides. Additionally, scattering-based transduction using plasmonic nanostructures can detect nanomechanical vibrations via shifts in optical resonances caused by motion at the nanoscale.

Besides detection, light can also be used for actuation via radiation pressure or photothermal forces. In particular, radiation pressure—derived from the momentum carried by photons—can drive resonators with forces in the piconewton range using milliwatt-scale laser powers. When enhanced using high-finesse optical cavities, this interaction becomes the basis of cavity optomechanics, which allows not only for actuation but also for ground-state cooling and quantum-level control of mechanical systems.

1.5.5 Frequency Tracking Schemes

Precise tracking of the resonance frequency is fundamental in nanomechanical sensing applications, as shifts in this frequency can indicate changes in mass, force, or environmental conditions. Various schemes have been developed to monitor these shifts, each with its own advantages and trade-offs.

Self-Sustained Oscillator (SSO)

An SSO utilizes the resonator's motion to sustain oscillations through a positive feedback loop. This method allows the system to oscillate at its natural resonance frequency without external frequency sweeping. SSOs are advantageous for their simplicity and low power consumption. However, their performance can be limited by the quality factor of the resonator and the stability of the feedback loop.

Phase-Locked Loop (PLL)

A PLL involves an external oscillator whose frequency is adjusted to match the phase of the resonator's output. This closed-loop system offers high precision and stability, making it suitable for applications requiring accurate frequency tracking. The complexity of PLLs is higher compared to SSOs, but they provide better control over the oscillation conditions.

Feedback-Free (FF) Scheme

The FF approach relies on open-loop measurements, where the resonator is driven near its resonance frequency, and the response is monitored without feedback. This method is straightforward to implement but may suffer from reduced sensitivity and stability, especially in noisy environments.

As discussed by Bešić et al., both theoretical and experimental studies have shown that while closed-loop approaches like the PLLO and self-adjusting SSO offer faster response times, they tend to exhibit reduced precision in environments with significant transduction noise when compared to the feedback-free scheme [78–80].

1.6 Sensitivity and Responsivity

The usefulness of nanomechanical resonators in sensing applications relies not only on their ability to oscillate and track resonance frequency, but also on how sensitively that frequency responds to external stimuli. This sensitivity is commonly quantified through the system's responsivity and its noise-equivalent power (NEP).

Sensitivity is quantified using the noise-equivalent power (NEP):

$$\mathrm{NEP} = \frac{\sqrt{S_y(\omega)}}{\mathcal{R}_P(\omega)}, \tag{1.5}$$

where:

- $S_y(\omega)$ represents the frequency noise power spectral density,
- $\mathcal{R}_P(\omega)$ represents the power responsivity [59],
- NEP measures the minimal absorbed power required to achieve a signal above the noise level.

Responsivity, defined as the ability of the sensor to convert an input signal (such as absorbed power) into a measurable output (frequency shift), is expressed as:

$$\mathcal{R}_P = \frac{\partial \omega_0}{\partial P}\frac{1}{\omega_0}H_{\mathrm{th}}(\omega) = \frac{\mathcal{R}_T(\omega)}{G}H_{\mathrm{th}}(\omega), \tag{1.6}$$

- $\mathcal{R}_T(\omega)$: Represents temperature responsivity,
- G: Denotes thermal conductance,

- $H_{\text{th}}(\omega)$: Refers to the low-pass transfer function [59]:

$$H_{\text{th}}(\omega) = \frac{1}{\sqrt{1 + \omega^2 \tau_{\text{th}}^2}},$$

Pre-stressed silicon nitride resonators amplify $\mathcal{R}_T$ by a factor proportional to E/σ, resulting in temperature response enhancements exceeding 1000 [11, 81].

Frequency Stability $S_y(\omega)$ is dictated by four primary noise sources [59]:

$$S_y(\omega) = S_{y,\text{th}}(\omega) + S_{y,\text{d}}(\omega) + S_{y,T}(\omega) + S_{y,\text{ph}}(\omega), \tag{1.7}$$

1. Thermomechanical noise arises from amplitude fluctuations, mitigated by maximizing resonator vibrational amplitude.
2. Detection noise originates from the readout system, requiring low-noise configurations.
3. Temperature fluctuation noise stems from thermal dissipation, minimized through high thermal conductance.
4. Photothermal back-action noise links light intensity fluctuations to frequency noise, significantly suppressed by photothermal enhancement.

The system's Limit of Detection (LoD), defined as the smallest quantity of an analyte that can be reliably detected but not necessarily quantified, is closely linked to NEP and photothermal heating.

1.7 NEMS-Based Infrared Spectroscopy

NEMS-IR is a relatively new analytical method that utilizes the photothermal effect for chemical sensing. The technique relies on NEMS resonators, usually made from pre-stressed silicon nitride, which function both as the sample holder and the sensor itself [24, 82]. These resonators are compatible with various sample deposition approaches [23], such as direct aerosol collection or drop casting, which provides flexibility in sample handling [82, 83].

When IR light is absorbed by particles on the resonators surface, the local heating that follows leads to thermal expansion and a reduction in the resonator's tension. This induces a shift in the resonant frequency of the resonator. The magnitude of this frequency shift is directly related to the amount of absorbed infrared (IR) energy. As demonstrated by

Bešić et al. [78, 84], the frequency shift is tracked through a closed-loop oscillation setup in combination with a frequency counter.

This method provides extremely high sensitivity, capable of detecting masses in the picogram range under ambient conditions. Moreover, it operates over a wide spectral range, from the UV to the far-IR [23], which allows it to be applied to a diverse array of samples, including nanoparticles [85, 86], pharmaceuticals [82, 87], thin polymer films [88], and even explosive residues [89]. In addition, a recent study has demonstrated its use with in-situ thermal desorption to separate analyte mixtures [24].

However, conventional NEMS–IR systems typically use tunable quantum cascade lasers (QCLs), which are narrowband, expensive, and require wavelength scanning to build a spectrum. This limits their practicality for broader applications.

To overcome these limitations, a new technique called NEMS–FTIR was introduced by Timarac-Popović et al. [90]. Instead of using a QCL, NEMS–FTIR combines the nanoelectromechanical membrane resonator with a commercial broadband FTIR spectrometer as a light source. This allows simultaneous analysis across the entire mid-IR spectrum in a single measurement. NEMS–FTIR preserves the high mass sensitivity of NEMS–IR but offers broader spectral coverage and simpler, more accessible instrumentation.

This technique was validated on a range of nanoplastics, including PS, PP, and polyvinyl chloride (PVC), where clear and distinct spectral peaks were observed even for sub-nanogram masses. The reported limits of detection were in the picogram range (353 pg for PS, 102 pg for PP, and 355 pg for PVC), highlighting the sensitivity of the method [90]. Spectral outputs matched well with conventional FTIR data but without the peak shifts typically associated with ATR–FTIR, making the results directly compatible with existing spectral databases.

In addition to its spectral accuracy and sensitivity, NEMS–FTIR demonstrated quantitative capabilities by enabling mass estimation of deposited particles based on their measured absorbance. The authors reported strong agreement between the expected and estimated masses of PS nanoparticles, validating the method's reliability for quantitative analysis [90].

Despite its high sensitivity and flexibility, NEMS–FTIR does have certain limitations. Very dilute samples may require pre-concentration. While techniques like multiple droplet deposition or nebulization can address this, they may introduce complexity in routine workflows. Additionally, in highly complex sample matrices, interference from organic background material may necessitate further sample clean-up or simplification [90].

1.8 Comparison of NEMS-Based Approaches with Traditional Spectroscopic Techniques

Traditional techniques such as FTIR and Raman spectroscopy remain widely used for microplastic analysis but face limitations at the nanoscale. FTIR is constrained by the diffraction limit, restricting its spatial resolution to approximately 10–20 μm [91], while Raman, although capable of sub-micron resolution, is susceptible to fluorescence interference and requires longer acquisition times [92, 93]. Even advanced approaches like SERS have only recently achieved detection of PS nanoplastics down to 50 nm with detection limits around 5–6 μg/mL [19, 20].

In contrast, NEMS-based IR techniques, particularly NEMS–FTIR, bypass the diffraction limit and offer picogram-level sensitivity. By combining nanomechanical resonance detection with broadband IR spectroscopy, NEMS–FTIR enables the detection, identification, and quantification of nanoplastics with minimal sample volumes. This makes it a powerful alternative to conventional methods, particularly for trace-level or early-stage degradation studies.

Chapter 2

Implementation

2.1 Experimental Setup for Accelerated Weathering

The accelerated weathering experiments were conducted to study the degradation behavior of three types of plastics: PA, PS, and PET.

For the study, PA samples were prepared from empty nylon 6 tea bags, while PS samples were obtained from coffee cup lids, and PET samples were cut from plastic bottles. PS and PET samples were cut into uniform rectangular pieces measuring 1 cm x 1 cm, as seen in previous studies on plastic degradation [44], to ensure consistent exposure during weathering, while the PA tea bags were left whole to preserve their original structure. The thin cotton string and small label attached to the tip of each tea bag were carefully removed using scissors.

The comprehensive classification of the prepared plastic samples, including their shapes, sizes, and sources, is presented in Table 2.1. These details provided a systematic approach for analyzing the deposition behavior and degradation patterns of each material type. The prepared plastic samples for the experiment, including PS lid pieces, PA tea bags, and PET bottle pieces, are shown in Figure 2.1.

The weights of seven pieces of each plastic type were measured during preparation using the Sartorius Entris II BCE64I-1S scale with a readability of 0.1 mg, ensuring accurate records for each sample placed into glass vials for subsequent removal at specific time intervals. These weights are summarized in Table 2.2. On average, the PS samples weighed approximately 0.07 g, PET samples weighed about 0.20 g, and PA tea bags weighed around 0.21 g.

All plastic samples, including PA tea bags, PS, and PET, were thoroughly washed three times with Milli-Q water to remove impurities or loose particles. After washing, all samples

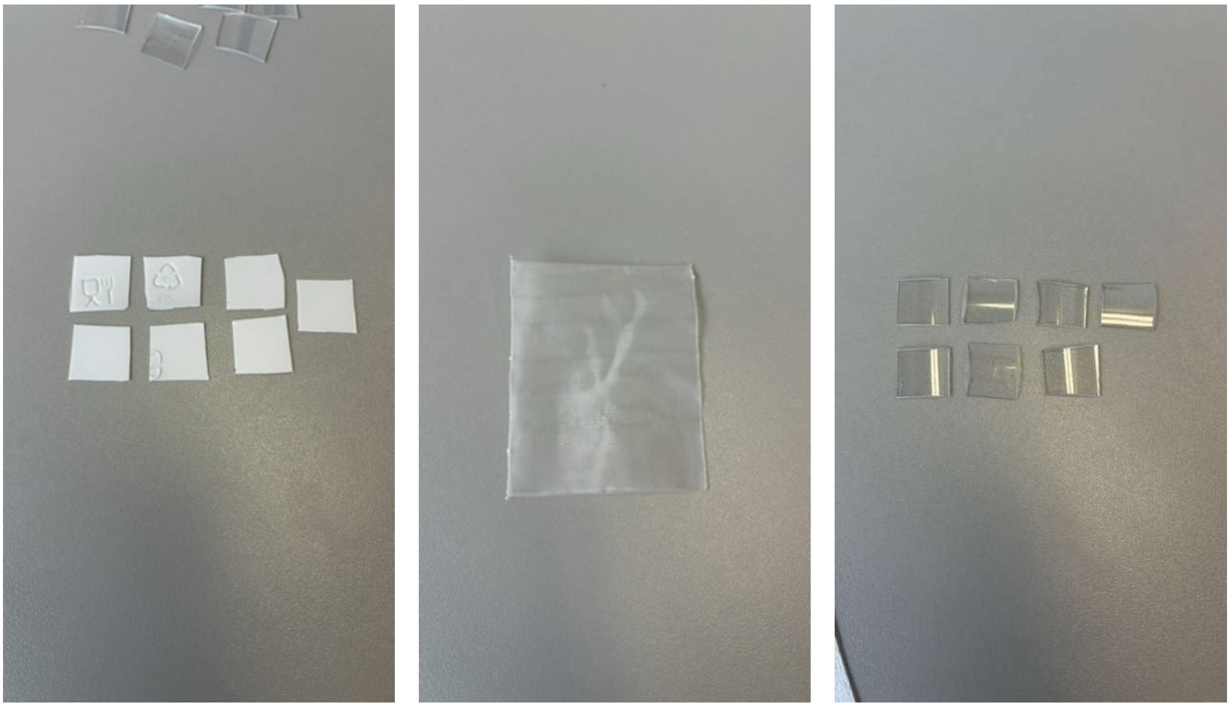

(a) (b) (c)

Figure 2.1: Prepared plastic samples for the accelerated weathering experiment: (a) PS lid cut into 1 × 1 cm^2 pieces; (b) PA tea bag after removal of the string and label; (c) PET bottle cut into 1 x 1 cm^2 pieces.

were allowed to dry overnight under a laminar flow hood (Secuflow, Waldner Holding, Germany).

Plastic particles corresponding to each material type were included in the experiment to examine nanoscale degradation processes. For all three materials (PA, PET, and PS), the particle concentration was standardized to 20 μg/mL to ensure consistency in the experiment. PS nanoparticles (100 ± 10 nm, 10% w/v in water) were obtained from Sigma-Aldrich (St. Louis, MO, USA). PA particles (5–50 μm) were purchased from Sigma-Aldrich (Product No. GF58818471, CAS No. 25038-54-4, Vienna, Austria). PET particles were initially provided by the Institute for Physical Chemistry of the Atmosphere at TU Wien, but were not included in the final experimental analysis.

The vials used were made of borosilicate glass (1st hydrolytic class), known for their high UV transparency, particularly in the UVA range, ensuring optimal UV exposure while minimizing light absorption. Each vial was filled with 30 mL of Milli-Q water to immerse the plastic samples during the weathering process. Screw caps constructed from

Table 2.1: Overview of the types of plastics used in this study, including their shapes, sizes, and sources.

Polymer	Shape	Size	Source
Polystyrene (PS)	Particle	100 ± 10 nm	Sigma-Aldrich
Polystyrene (PS)	Piece	1 cm × 1 cm	Coffee lid
Polyamide (PA)	Particle	5-50 µm	Sigma-Aldrich
Polyamide (PA)	Piece	7 ± 0.3 cm × 6 ± 0.3 cm	Tea bag
Polyethylene Terephthalate (PET)	Particle	Unknown	IPCA TU Wien
Polyethylene Terephthalate (PET)	Piece	1 cm × 1 cm	Bottle

Table 2.2: Weights of plastic samples during preparation.

Day	PS Lid [g]	PET Bottle [g]	PA Tea Bag [g]
1	0.0731	0.1947	0.2098
2	0.0732	0.2213	0.2098
5	0.0703	0.1796	0.2129
10	0.0607	0.1899	0.2189
15	0.0527	0.1866	0.2094
20	0.0727	0.1825	0.2090
25	0.0750	0.1705	0.2123

PP with silicone/PTFE seals were used, offering resistance to both UV radiation and high temperatures while maintaining a leak-proof environment. The prepared glass vials containing the plastic samples, ready for placement in the climate chamber, are shown in Figure 2.2.

Figure 2.2: Prepared glass vials containing PS, PET, and PA plastic samples (pieces and particles) immersed in 30 mL of Milli-Q water, labeled for the sampling intervals.

During the preparation process all glass vials and screw caps were washed similarly to the plastic samples, three times with Milli-Q water, and then dried under a laminar flow hood to ensure cleanliness. Nitrile gloves (Kowloon, Stronghand disposable gloves, Helmut Feldtmann GmbH, Germany) were worn at all times to ensure proper handling of the plastic samples and glassware. Each glass vial was labeled using a marker to indicate the plastic type and sampling day, ensuring accurate identification throughout the experiment.

The weathering process was carried out in a SimTech Feutron Double Climate Chamber with internal dimensions of 73 cm x 77 cm x 102 cm. The chamber is designed for precise environmental control, allowing fine-tuned temperature and UV exposure settings. It is equipped with a programmable digital controller that regulates temperature, light intensity, and exposure cycles.

Two Osram Ultra-Vitalux lamps (model 4008321543929, 300W, 230V, E27), positioned 30 cm apart at the top of the chamber, provided the UV radiation source. The lamps were installed externally in the chamber, and their operation was controlled using a programmable timer switch, ensuring precise on-and-off cycles during the experiment. These high-pressure mercury vapor lamps emit a broad spectrum of UV radiation, with significant output in the UVA (315–400 nm) and UVB (280–315 nm) ranges, closely simulating natural solar radiation. Their approximate irradiance was measured at 59.1 W/m^2 using a Conrad Chromameter and confirmed through calculations, ensuring effective photodegradation comparable to long-term outdoor exposure.

A fixed metal plate was positioned 32 cm below the lamps to securely hold the glass vials containing the plastic samples. The arrangement of the glass vials within the climate chamber, alongside the positioning of the lamps, is shown in Figure 2.3, providing a detailed visualization of the experimental setup.

The internal environment of the chamber was maintained using precision-controlled airflow, ensuring consistent temperature distribution and even UV exposure. Additionally, the system featured an advanced cooling mechanism to prevent overheating during prolonged UV exposure cycles.

The climate chamber was programmed on a cyclic schedule to replicate natural environmental conditions. Each cycle comprised 8 hours of UV exposure at 60°C, followed by 4 hours of darkness at 25°C, facilitating thermal fluctuations similar to real-world day-night cycles. These parameters were selected following internationally recognized standards ISO 4892-3 [50] and ASTM G154 [51], which recommend such regimes for simulating natural weathering processes. The climate chamber programming interface, depicted in Figure 2.4, details the cyclic schedule implemented to simulate natural environmental conditions. The

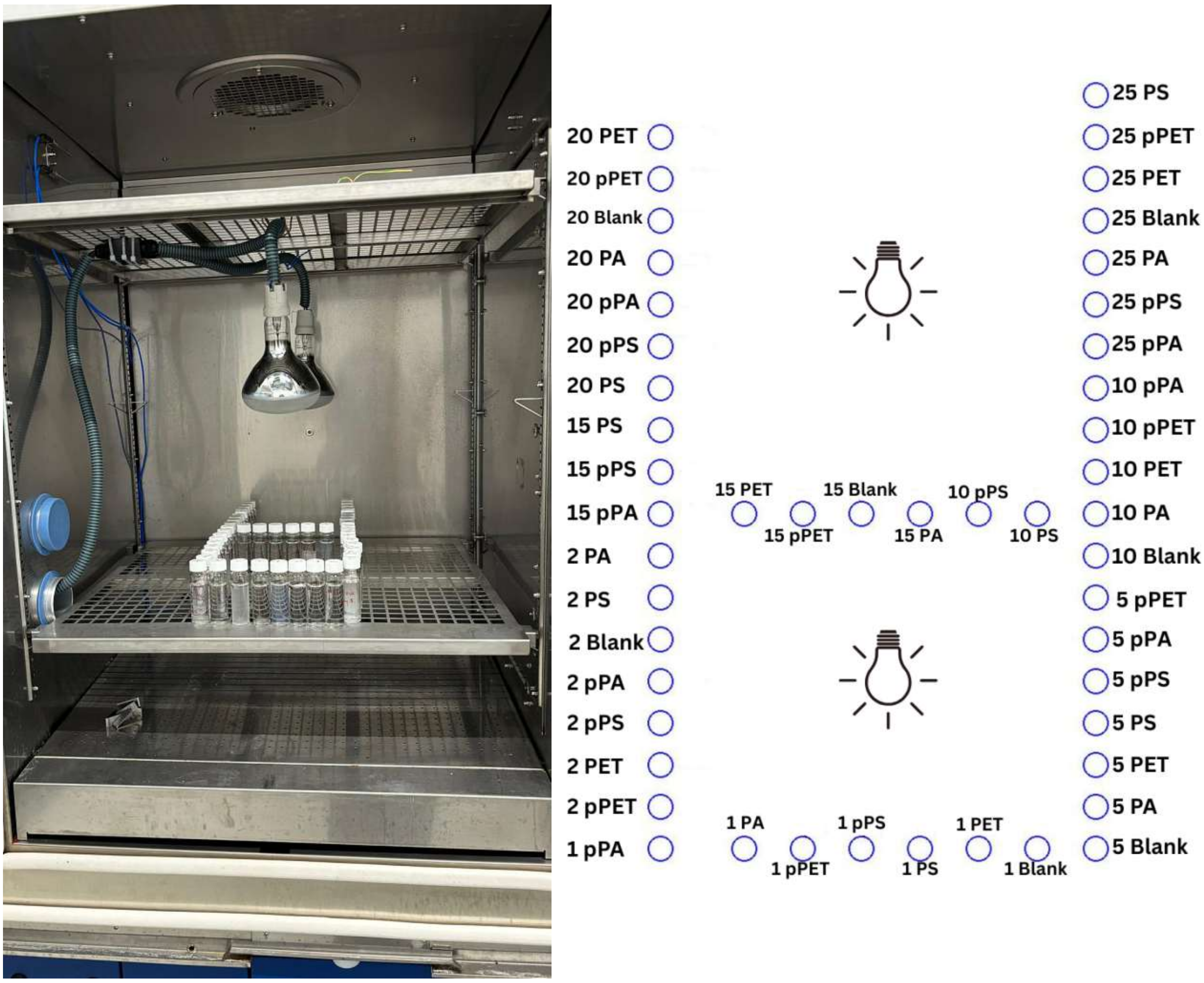

Figure 2.3: (Left) Climate chamber setup, showing the UV lamps and glass vials positioned on the metal plate. (Right) Diagram illustrating the arrangement of glass vials inside the chamber for uniform UV exposure.

specific settings of the climate chamber, including radiation, temperature, and exposure duration, used for the artificial aging of plastic samples are detailed in Table 2.3.

Table 2.3: Experimental conditions set in the climate chamber for the artificial aging process of plastic samples.

Radiation	**Wavelength**	**Temperature**	**Irradiance**
UV	280–400 nm	60°C (UV), 25°C (No UV)	8 h (UV), 4 h (No UV)

The total experimental period lasted for 25 days, which, according to Mathew Philip and Farah Al-Azzawi [48], corresponds approximately to one year of natural weathering under

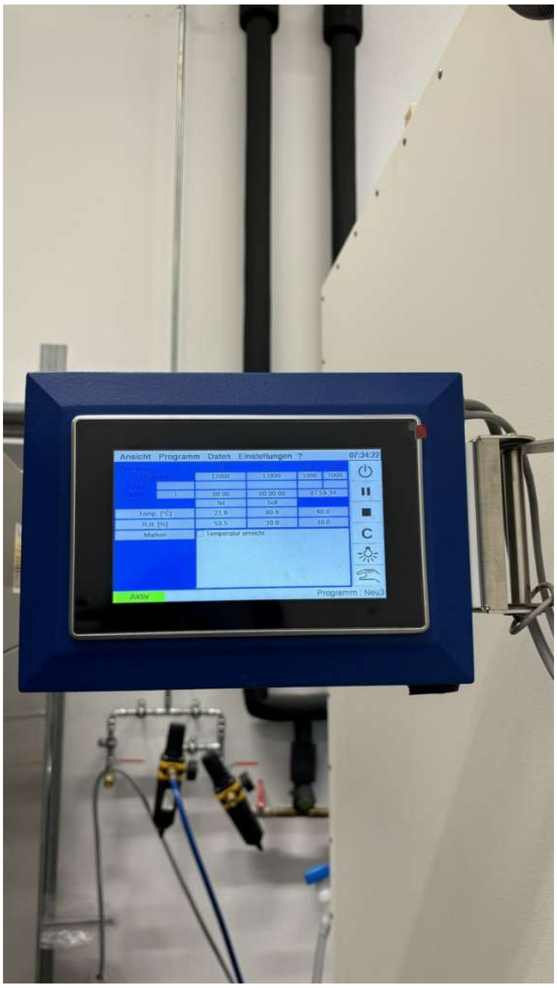

Figure 2.4: Programming interface of the climate chamber, illustrating the cyclic schedule for UV exposure (8 hours at 60°C) and dark recovery (4 hours at 25°C).

comparable UV intensities and exposure conditions. Throughout the experiment, plastic samples were periodically monitored, with selected vials removed at specific time intervals: after 1, 2, 5, 10, 15, 20, and 25 day(s), allowing a detailed investigation of degradation progression over time.

2.2 Sample Collection and Preparation

To prepare water samples for analysis, three distinct sampling methods were explored: manual dropcasting, nanodropper-based deposition, and a nebulizer setup. Each method had unique advantages and disadvantages, which are detailed below, followed by a description of how they were applied during the experiment.

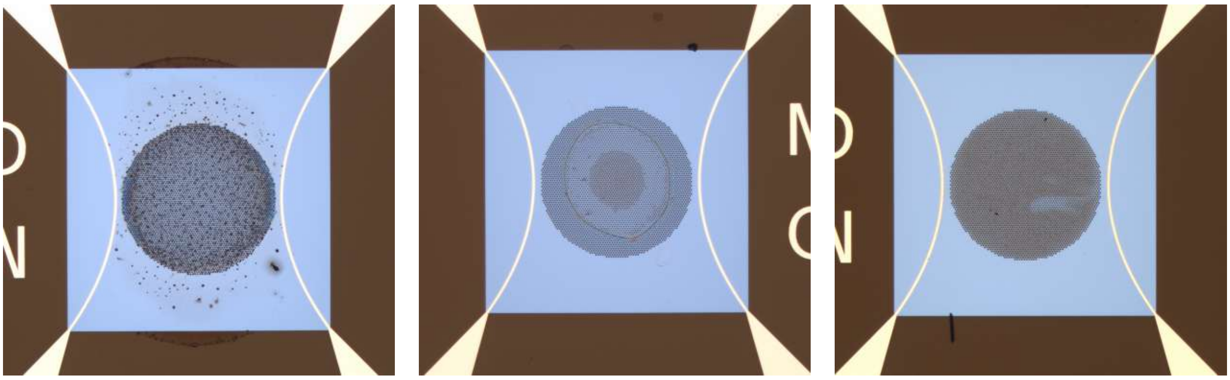

(a) (b) (c)

Figure 2.5: Microscopic images of NEMS chips after sample deposition using (a) manual dropcasting, (b) nanodropper, and (c) nebulizer, showing differences in distribution uniformity and drying artifacts.

2.2.1 Manual Dropcasting

When the experiment began, manual dropcasting was employed as the initial sampling method due to its simplicity and ease of use. Manual dropcasting involved using a precision pipette (Pipetman P2, Gilson Incorporated, WI, USA; volume range 0.2–2 μL) with matching DIAMOND tips to deposit 1 μL of the prepared sample directly onto the central perforated area of the chip. The key advantage of manual dropcasting was its straightforward implementation, making it ideal for preliminary experiments. However, significant limitations became apparent during its application. The droplet often failed to dry uniformly on the membrane, leading to inconsistent particle distribution. Microscope images revealed uneven deposition, with some areas of the membrane overloaded while others remained uncovered. Figure 2.5a shows an example of this non-uniform coverage, where particle clustering and bare spots are clearly visible on the membrane.

The need to wait for the liquid to fully dry, taking up to an hour for a 1 μL pipetted sample, further reduced the practicality of the method for large-scale preparation. The inconsistency compromised the reliability of subsequent analyses and underscored the limitations of this method for achieving homogeneous coverage.

2.2.2 Nanodropper-based Deposition

The nanodropper method was the next approach tested to improve sample deposition consistency. The nanodropper used in this step was the PIPEJET nanoDispenser (BioFluidix–Hamilton, Freiburg, Germany), equipped with a polyimide capillary (inner diameter: 200 μm, Prod. No. PJ–20010) and a 1 cm piece of Tygon tubing (Prod. No. VM–20053–1). Droplets of precisely 20 nL were deposited onto the center of the NEMS chip, with the stroke velocity set to 90 μm/ms. This method offered greater control over droplet size and placement, allowing for more uniform deposits on the chip's surface. The nanodropper also minimized the risk of sample loss. Despite these advantages, the method proved to be highly time-intensive, as each sample required meticulous handling and precise adjustments. Furthermore, to achieve a total deposited volume of at least 1 μL, needed to increase the sample mass on the chip for improved detectability, it was necessary to dispense 50 droplets of 20 nL each. A mandatory 2-minute pause between droplets was required to ensure complete drying and accurate placement of subsequent drops. As a result, the deposition of a single sample could take over 1.5 hours, making this method impractical for the scope of the study. While it addressed some issues encountered with manual dropcasting, its labor-intensive nature and limited scalability restricted its broader application. The resulting deposition pattern can be seen in Figure 2.5b, where the droplet rings are visible, indicating controlled but time-intensive application.

2.2.3 Nebulizer Setup

The nebulizer setup emerged as the most advanced and efficient sampling method. Designed to aerosolize liquid samples, the nebulizer converted the sample into a fine mist, which was then deposited onto the NEMS chips. The process involved passing the liquid through a central capillary surrounded by pressurized air, creating a consistent aerosol. The inclusion of a spray chamber further refined the aerosol by removing larger droplets, ensuring only fine particles reached the chip. This method provided uniform sample coverage and proved to be highly reproducible across multiple trials. The resulting deposition pattern is shown in Figure 2.5c, illustrating the uniform and homogeneous sample distribution achieved with this method. Although the setup required precise calibration and additional equipment, such as flow meters and a diffusion dryer, its ability to handle large sample volumes efficiently made it the most suitable choice for the experiment. After evaluating the advantages and disadvantages of all three approaches, the nebulizer setup was adopted as the primary sampling technique for the remainder of the experiment.

Nebulizer Setup: Detailed Explanation

Several deposition mechanisms govern particle capture in aerosol systems, including inertial impaction, interception, and Brownian diffusion [94]. In our setup, NEMS chips are specifically designed with an array of submicron perforations (6 μm in diameter, spaced 3 μm apart) distributed across a circular area of 600 μm in diameter. When a flow rate of 1 L/min is applied using the pump, the resulting air velocity through the perforated membrane reaches approximately 109 m/s [95]. Under these conditions, particle deposition is dominated by inertial impaction, a mechanism particularly effective at high flow velocities and discussed in greater detail by Schmid et al. [96].

The nebulizer setup, illustrated in Figure 2.6, was composed of several key components that worked together to ensure efficient aerosolization and deposition of liquid samples onto the NEMS chips:

1. Syringe pump: A precision syringe pump was used to deliver the liquid sample to the nebulizer at a controlled flow rate of 10 μL/min. This ensured a consistent and steady supply of the sample, critical for maintaining uniform aerosol production.

2. Nebulizer: The nebulizer served as the central component of the setup, atomizing the liquid into a fine aerosol. Pressurized air (0.45–0.50 L/min) was directed through the nebulizer, creating shear forces that broke the liquid into micron-sized droplets.

3. Spray chamber: Downstream of the nebulizer, a spray chamber removed larger droplets from the aerosol stream via a waste line. This step refined the aerosol, ensuring that only fine, uniformly sized droplets were deposited onto the chip.

4. Inline filters: Inline filters cleaned the pressurized air entering and exiting the system, preventing potential contamination of either the sample during aerosolization or the surrounding environment.

5. Diffusion dryer: The aerosol passed through a diffusion dryer to remove excess moisture, ensuring that only dry particles reached the chip.

6. Flow meters: Flow meters were strategically placed throughout the setup to monitor and regulate air flow rates. Precise control of these parameters was essential for achieving optimal aerosolization and deposition.

7. Aerosol Flow Adapter: The Aerosol Flow Adapter (Invisible-Light Labs GmbH, Austria) was used to securely position the NEMS chip during aerosol-based sample deposition. It ensured correct alignment of the aerosol stream with the membrane surface and protected the delicate chip from mechanical disturbance during handling. The setup enabled consistent and reproducible deposition by maintaining the chip in a fixed and stable position throughout the sampling process. An image of the adapter in use is provided in Figure 2.7.

8. Pump: A vacuum pump maintained the airflow required to drive the aerosol through the system. The pump ensured that the aerosol stream passed effectively through the chip, facilitating consistent and complete deposition. The flow rate was maintained at 0.7 L/min during the entire sampling process to ensure optimal particle transport and uniform deposition.

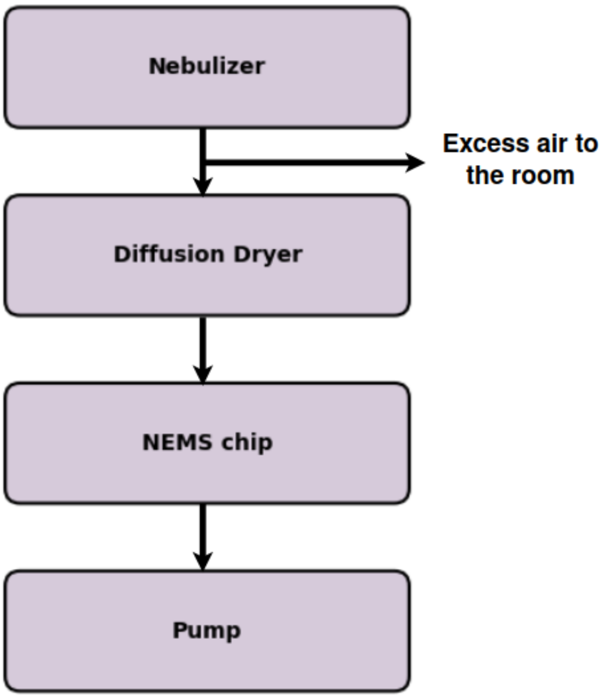

Figure 2.6: Schematic of the nebulizer setup used for sample preparation, including key components such as the syringe pump, nebulizer, spray chamber, and EMILIE™ sampler.

Figure 2.7: The aerosol flow adapter used to securely position the NEMS chip during the sample deposition [97].

2.2.4 Implementation in the Experiment

In the nebulizer setup, specific sampling durations were established for different particle types to ensure optimal deposition and prevent overloading of the resonator. Aqueous extracts obtained from PS lid, PS particle, PA particle, and PA teabag dispersions were aerosolized using a syringe pump operating at 10 μL/min, with respective deposition times of 7, 3, 5, and 5 minutes. These durations were determined based on preliminary experiments to balance uniform coverage and adequate mass deposition while maintaining the operational efficiency of the EMILIE™ chips.

Additionally, for each sample, the system was allowed to run for at least 10 minutes before sampling began to ensure that the entire system was adequately flushed and stabilized.

Initially, triplicates were prepared for each sample, including blanks for each day, to ensure robust data collection and reproducibility. However, due to the high number of chips required for this experiment, the protocol was adjusted to duplicates to conserve resources while maintaining reliable cross-verification.

All chips were handled with clean gloves and precision tweezers to avoid contamination and physical damage to the delicate membranes. After sampling, the chips were stored in chip-boxes with lid to protect them from dust, moisture, and other external elements. At least two chips were sampled for each experimental condition, allowing for cross-verification of results and minimizing the impact of outliers.

As part of the process, each chip was inspected under a microscope before proceeding with further analysis to ensure that the samples were properly dried exactly on the membrane. The microscope used for this step was a Leica DM6000 M Automated Research Microscope for Materials Science, which enabled precise inspection of sample placement and surface coverage. This step was critical to verify the quality of the sample preparation and prevent inconsistencies in the experimental results.

The efficiency and reproducibility of the nebulizer setup were instrumental in ensuring the success of the study. Its ability to produce uniform sample coverage allowed for the reliable detection of nanoplastics, even at low concentrations.

Filtration Steps

For PA samples, an additional filtration step was implemented prior to deposition. This was necessary because the PA particles used in this study ranged from 5 to 50 μm in diameter. Given the high air velocities in the system, the direct impact of such large particles posed a significant risk of mechanical damage or even membrane rupture. By filtering out the larger fragments, only smaller particles were deposited onto the chip, reducing the risk of structural failure and ensuring that the resonator remained within its operational limits.

Polycarbonate membrane filters (disk diameter 19 mm, pore size 30 nm) manufactured by Whatman were used for this purpose. As the original PA particles were significantly larger than the filter pore size, they were entirely retained during filtration. Therefore, any particles detected after this step can be attributed to degradation products resulting from the weathering process. This ensured that the material analyzed on the chip consisted exclusively of nanoscale fragments, eliminating interference from intact, unweathered particles.

2.3 Obtaining Spectra using NEMS-FTIR

Following the sample preparation and deposition, the detection and identification of nanoplastics were carried out using the nanoelectromechanical infrared (IR) analyzer (EMILIE^{TM}, Invisible-Light Labs GmbH, Austria), coupled with a Bruker Vertex 70 FTIR spectrometer (Bruker Optics GmbH, USA). This integrated system, as thoroughly explained in previous sections, combines the high sensitivity of nanoelectromechanical resonators with the broad spectral capabilities of a commercial FTIR source, allowing for precise detection of low-mass analytes such as nanoplastics.

The pre-stressed SiN membrane of the NEMS chip functioned both as a sample holder and as a detector. When the deposited analyte absorbed IR radiation, localized photothermal heating occurred, leading to a reduction in membrane tension and a corresponding shift in its resonance frequency. These frequency shifts were tracked using a closed-loop, self-sustained oscillator (SSO) circuit integrated into the EMILIE™ system. The frequency changes were continuously converted into voltage signals and sent to the spectrometer, enabling the system to generate IR spectra representative of the analyte's molecular composition.

A schematic of the experimental setup is shown in Figure 2.8. Each sample-loaded NEMS chip was placed into the vacuum chamber, where the internal pressure was maintained at 10^{-5} mbar to eliminate spectral interference from ambient gases and to minimize mechanical noise, thereby enhancing the sensitivity and stability of the measurement. To ensure thermal stability during measurements, the chip temperature was actively regulated to 25 °C using an integrated thermoelectric cooler (TEC) in combination with a Peltier element.

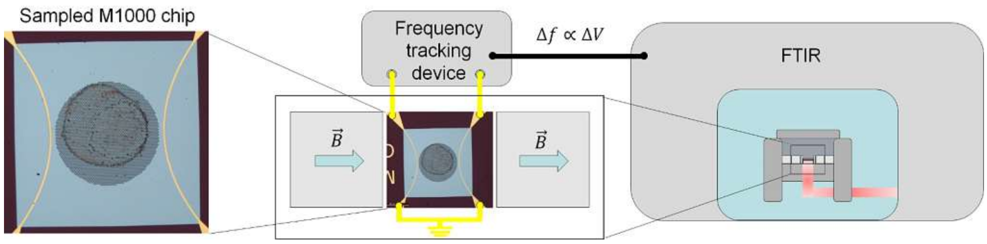

Figure 2.8: Schematic representation of the NEMS–FTIR setup used in this study. The sampled chip is placed in a magnetic field and connected to a frequency tracking device, which monitors resonance frequency shifts (Δf) and converts them into a change in output voltage (ΔV) which is then sent to the FTIR. The system is coupled to a commercial FTIR spectrometer, which serves as the broadband infrared light source.

The FTIR acquisition parameters were configured as follows:

- **Spectral range:** 4000 to 400 cm^{-1}
- **Spectral resolution:** 4 cm^{-1}
- **Number of co-added scans:** 200
- **Aperture:** 6 mm
- **Stabilization delay:** 30 ms

To ensure accurate interpretation, blank measurements were recorded under identical conditions using chips sampled with distilled deionized water (DDW, 18 MΩcm; Millipore, MA, USA) that went through the same accelerated weathering process. These spectra were subtracted from sample spectra during post-processing to remove background signals. The resulting spectral data were further analyzed as described in the following section.

2.4 Data Analysis and Interpretation

The background-corrected spectral data were processed and analyzed using a custom Python-based workflow implemented in Jupyter Notebook. This workflow was applied consistently to all sample types and time points, with modifications only where necessary to account for spectral differences between materials.

As a first step, each raw spectrum was normalized by dividing it by the NEMS-FTIR spectrum of the light source to correct for the wavelength-dependent intensity distribution. The light source spectrum was recorded using a NEMS chip coated with a 5 nm ultra-thin platinum film (EMILIE™ LIGHT chip, Invisible-Light Labs GmbH, Austria), which functions as a broadband IR absorber [98].

Following light source correction, the spectra of blank samples were subtracted from the corresponding analyte spectra to isolate signals originating from the polymeric particles. To further reduce high-frequency noise while preserving relevant spectral features, optional smoothing was applied using a Savitzky–Golay filter (typically with a window length of 20 and a polynomial order of 2).

All measurements were organized as instances of the `MeasurementSet` class, which encapsulates both raw and processed data. For each polymer, a set of characteristic wavenumber regions was predefined based on literature references and prior results. Within each region of interest, peak tracking was conducted using a custom peak-detection algorithm, extracting the maximum intensity within a specified window (typically $\pm 20\,\mathrm{cm}^{-1}$). The extracted peak intensities were then used to assess temporal trends in signal development throughout the aging period.

The following types of visualizations and analyses were performed:

- Overlays of all time-point spectra were generated to facilitate visual comparison and to observe spectral changes throughout the experiment.

- Inset plots were used to zoom in on specific spectral regions where relevant differences or trends were observed.

- Time-resolved plots of extracted intensity values were created to monitor trends such as signal stability, increase, or decrease over time.

To aid interpretation, vertical lines were drawn at characteristic wavenumbers for each material. All spectra were plotted with consistent line styles and colors to clearly differentiate between time points. Exported plots were saved in vector formats (PDF and SVG) for publication-quality figures and reproducibility.

This workflow allowed both qualitative inspection of spectral features and quantitative tracking of peak intensity across different days. The same processing and analysis structure was applied to all polymers, ensuring comparability while accounting for the unique spectral properties of each material.

Chapter 3

Results and Discussion

All measured samples, regardless of polymer type or origin, were processed using the same NEMS–FTIR technique described in Chapter 2. Each sample type was monitored over time to track spectral changes induced by the accelerated aging process.

Before discussing the spectroscopic findings, this chapter first presents the macroscopic changes observed during weathering. These include visual degradation and mass loss, which offer essential context for interpreting the chemical transformations detected through NEMS–FTIR.

The results are presented in the following order:

- Macroscopic changes and mass loss
- PA teabag samples
- PA particles
- PS lid samples
- PS particles

For each group, key spectral features are highlighted and tracked over the aging period. Visualizations are accompanied by extracted intensity values at selected wavenumbers to enable comparison and interpretation. This structure allows for both individual material evaluation and broader observations across different plastic types.

PET samples were excluded from further experimental steps primarily to optimize time and resources. Among the tested polymer types, PET is known to degrade the slowest under environmental conditions, making it a less suitable candidate for studies focused on early-stage degradation products. While some challenges in deposition consistency were observed, they were not the main reason for its exclusion. Instead, the decision was driven by the limited experimental capacity and a strategic focus on materials (e.g., PS and PA) that exhibit faster degradation and are thus more relevant for the scope of this work.

3.1 Macroscopic Changes and Mass Loss

To complement the spectroscopic analysis presented later in this chapter, the physical degradation of the polymer samples was also examined through direct visual inspection and mass measurements at each time point during the accelerated weathering process.

Visual Appearance of Weathered Plastics

To visually assess degradation, photographs were taken before and after the weathering process. The initial condition of the plastic samples is shown in the previous chapter, in Figure 2.1, which shows their appearance before the start of the accelerated aging experiment. The post-weathering state of the same materials after 25 days of UV exposure and thermal cycling is shown in Figure 3.1. For each polymer type, the samples are arranged from left to right in chronological order, starting with Day 1 and ending with Day 25, to illustrate the progression of physical degradation over time.

(a) (b) (c)

Figure 3.1: Plastic samples after 25 days of accelerated weathering under UV exposure and thermal cycling: (a) PS lid pieces; (b) PET bottle fragments; (c) PA tea bag material. For each polymer type, one sample per day is shown, arranged from left (Day 1) to right (Day 25), illustrating the chronological progression of physical degradation.

The PS lid pieces (Figure 3.1a) exhibited the most pronounced visible changes. During the first few days (Days 1–5), no significant alterations were observed. However, on day 10, yellowing became apparent and progressively intensified on days 15, 20, and 25. In addition to discoloration, the samples became noticeably brittle and fragile, easily breaking apart during handling, a characteristic indication of photooxidative degradation in polystyrene [27].

The PET bottle fragments (Figure 3.1b) exhibited pronounced shape deformation. All samples appeared curled and warped, even from the earliest time points. Despite the noticeable physical change, it was, as previously mentioned, difficult to obtain consistent and meaningful spectral data from PET samples.

In contrast, the PA tea bag material (Figure 3.1c) showed no significant optical changes throughout the 25-day period. The samples remained structurally intact, with no apparent discoloration, fraying, or deformation. This suggests that PA exhibited the greatest resistance to the applied weathering conditions in terms of visible physical degradation.

Mass Loss During Weathering

Mass measurements were recorded at each sampling point to quantitatively monitor potential material loss as a physical indicator of degradation (Tables 2.2 and 3.1). However, the results did not show a clear or consistent trend for all polymers.

Table 3.1: Weights of plastic samples after the accelerated weathering process.

Day	PS Lid [g]	PET Bottle [g]	PA Tea Bag [g]
1	0.07294	0.19542	0.20648
2	0.07228	0.22280	0.20620
5	0.07280	0.18047	0.20924
10	0.06153	0.19251	0.21392
15	0.05258	0.18741	0.20392
20	0.07359	0.18334	0.20472
25	0.07532	0.17161	0.20721

For the PS lid samples, the measured masses fluctuated slightly, with a minor decrease up to Day 15 followed by a slight increase by Day 25. This pattern suggests that while initial degradation may have occurred, subsequent weight gain could be attributed to water absorption, surface contamination, or incomplete drying before measurement. As such, no definitive mass loss could be confirmed for PS.

The PET bottle fragments, in contrast, showed a small but consistent increase in mass across all measured time points. This gain is likely due to swelling or residual water retention within the polymer matrix, rather than any form of degradation. These findings align with visual observations, where PET underwent physical deformation (curling) but showed no progressive fragmentation or discoloration.

Among the three polymer types, PA tea bag samples were the only ones to show a consistent decrease in mass over time. From Day 1 to Day 25, a small but measurable reduction in weight was observed, which may reflect subtle fiber degradation or leaching under the applied UV and thermal conditions.

Overall, due to variability in measurements and possible interference from environmental factors such as humidity and drying, these mass values are not used as the primary indicator of degradation. Instead, they serve as supplemental information alongside the more reliable spectroscopic results.

3.2 PA Teabag Samples

This section examines the spectral changes observed in the aqueous extracts obtained from PA teabags soaked in water over a period of 25 days under accelerated weathering conditions. FTIR spectra were analyzed to monitor characteristic vibrational bands associated with structural changes in the polymer matrix. Assignments and interpretations are based on established literature describing thermal and oxidative degradation, crystallinity behavior, and hydrogen bonding dynamics in PA6 materials [99–104]. The results are presented using five figures, including an overview spectrum of all time points and four detailed plots focusing on critical vibrational regions relevant to PA degradation.

Figure 3.2 shows an overview of the normalized NEMS–FTIR spectra over the full mid-infrared range. Several key regions were identified as undergoing notable changes with increasing exposure duration: the N–H stretching region (3300 cm^{-1}), the aliphatic C–H stretching region (2930 cm^{-1}), and the amide I and II bands (1640 and 1535–1540 cm^{-1}, respectively). These bands are well-established markers of polyamide chemistry and are sensitive to environmental and thermal stress [100, 102].

Figure 3.3 highlights the evolution of the N–H stretching band. The increasing peak intensity suggests enhanced hydrogen bonding, which may result from oxidative functionalization or water sorption under weathering conditions [102–104]. Similar spectral changes were reported in studies involving PA6 subjected to UV, moisture, and thermal aging [104].

Figure 3.4 highlights the spectral changes in the amide I region, centered near 1640 cm^{-1}, which corresponds to the C=O stretching vibration in the polyamide backbone [100, 102].

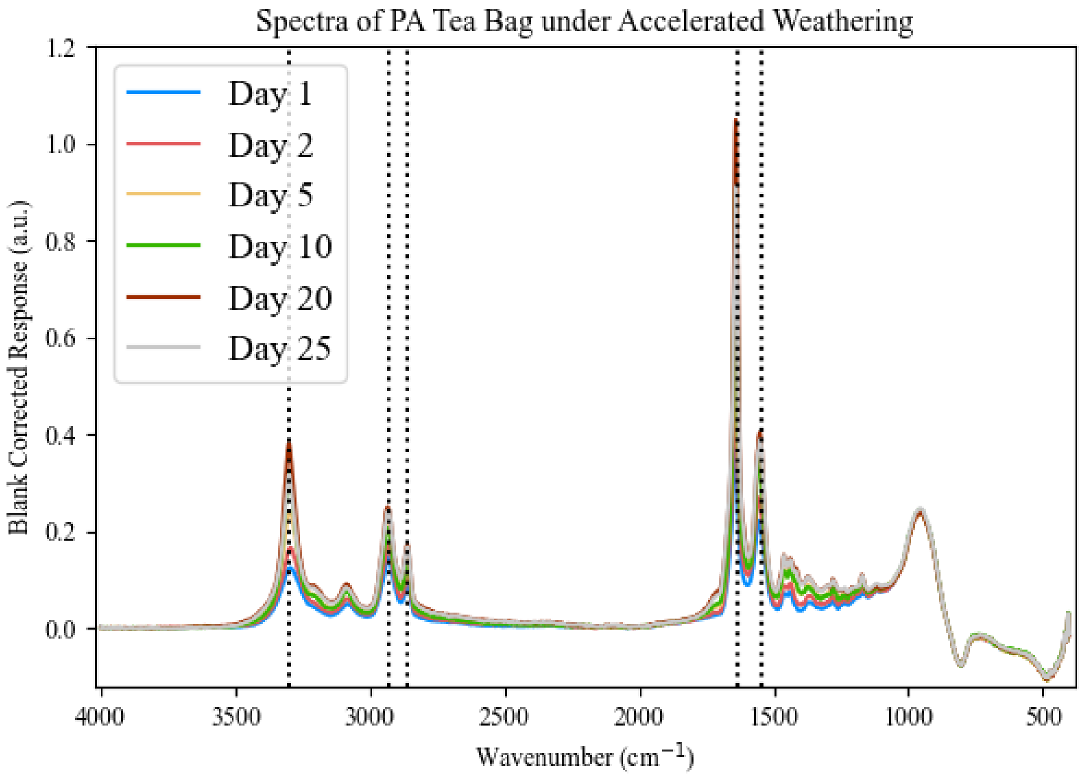

Figure 3.2: NEMS–FTIR spectra of aqueous extracts obtained from PA teabags immersed in water during 25 days of artificial weathering.

A gradual increase in peak intensity is observed over the weathering period, consistent with oxidative degradation and the accumulation of carbonyl-containing byproducts such as aldehydes and ketones [99, 101]. Changes in hydrogen bonding environments have also been linked to crystalline transformations and variations in FTIR spectral bands in polyamide 6 [100]. These trends align with previously reported findings in thermally and environmentally aged PA6 materials [104].

Figure 3.5 focuses on the amide II region (1550 cm^{-1}), which primarily corresponds to N–H bending and C–N stretching vibrations in polyamide structures [102]. While typically less intense than the amide I band, the amide II region also reflects structural changes observed during polyamide aging [99, 104].

Changes in the amide II band further support the observed trend of oxidative degradation, complementing the evolution of the amide I region and reinforcing the progressive nature of molecular modifications in PA6 during weathering [99, 104].

Figure 3.6 shows the spectral behavior in the aliphatic C–H stretching region (2900–

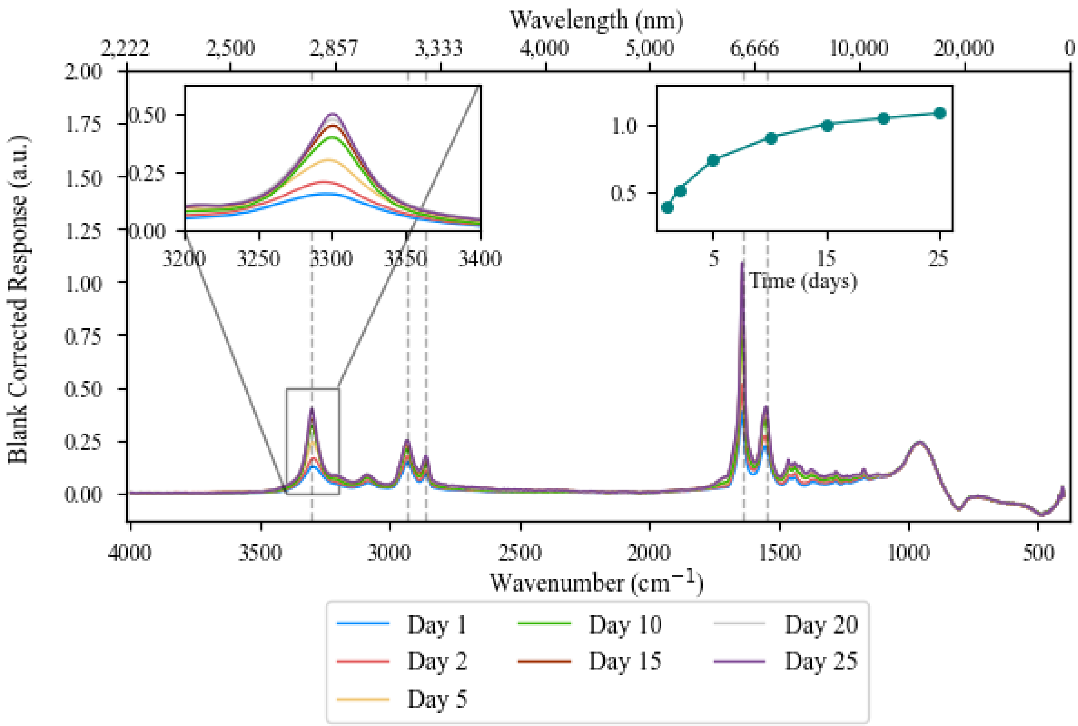

Figure 3.3: NEMS–FTIR spectra of aqueous extracts obtained from PA teabags, highlighting the N–H stretching region. The zoomed-in inset shows the evolution of peak intensity in the 3200–3400 cm^{-1} range.

3000 cm^{-1}), which includes characteristic vibrations of methylene groups. In polyamide 6, Liu et al. [105] identified peaks at 2932 cm^{-1} and 2854 cm^{-1} as corresponding to $-CH_2-$ stretching.

Although this region is less emphasized in polyamide degradation studies, a moderate increase in peak intensity near 2932 cm^{-1} is observed during the artificial weathering period.

In summary, NEMS–FTIR analysis of aqueous extracts from weathered PA teabags revealed progressive spectral changes across key vibrational regions. Increased intensity in the N–H, amide I, and amide II bands indicates moisture uptake and oxidative modification of the polymer backbone [99,101,102,104]. Additional changes in the CH_2 stretching region support gradual chemical alteration of the matrix [105]. These findings, obtained without sample pre-concentration or filtration, highlight the sensitivity of the NEMS–FTIR method for monitoring polyamide degradation.

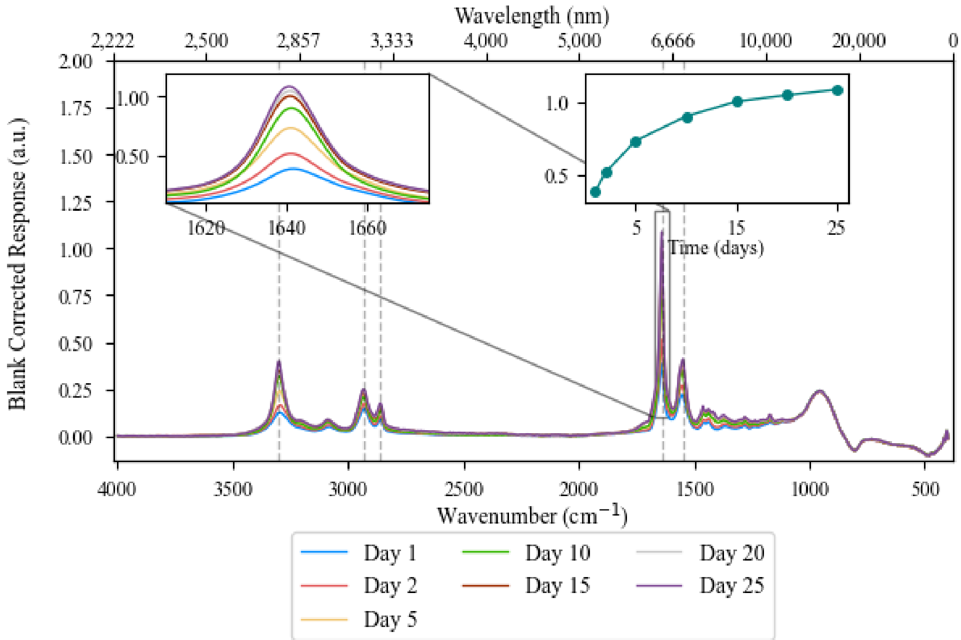

Figure 3.4: NEMS–FTIR spectra of aqueous extracts obtained from PA teabags, highlighting the amide I region. The zoomed-in inset shows the evolution of peak intensity in the 1600–1700 cm^{-1} range.

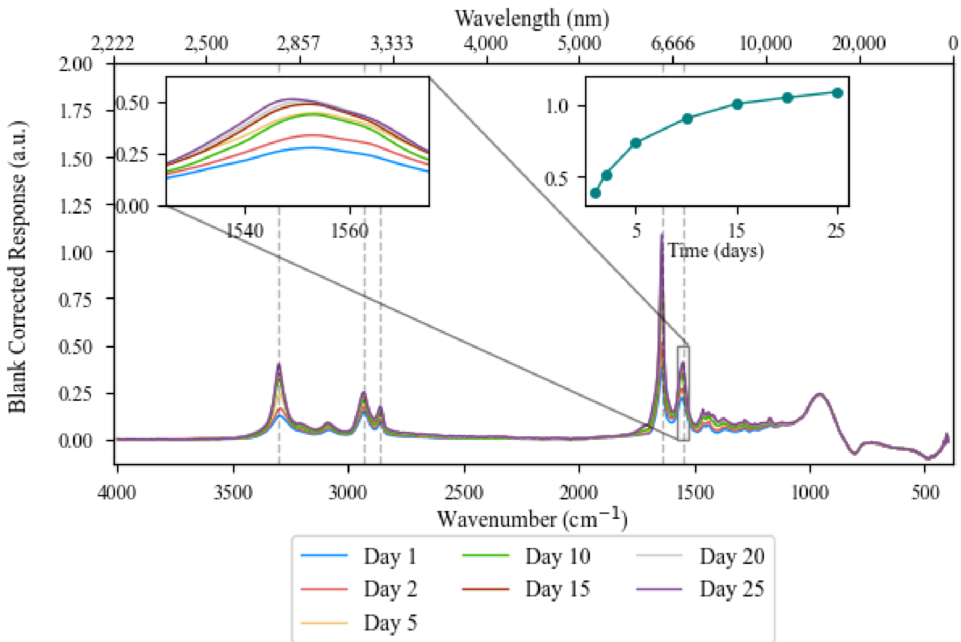

Figure 3.5: NEMS–FTIR spectra of aqueous extracts obtained from PA teabags, highlighting the amide II region. The zoomed-in inset shows the evolution of peak intensity centered at 1550cm^{-1} during artificial weathering.

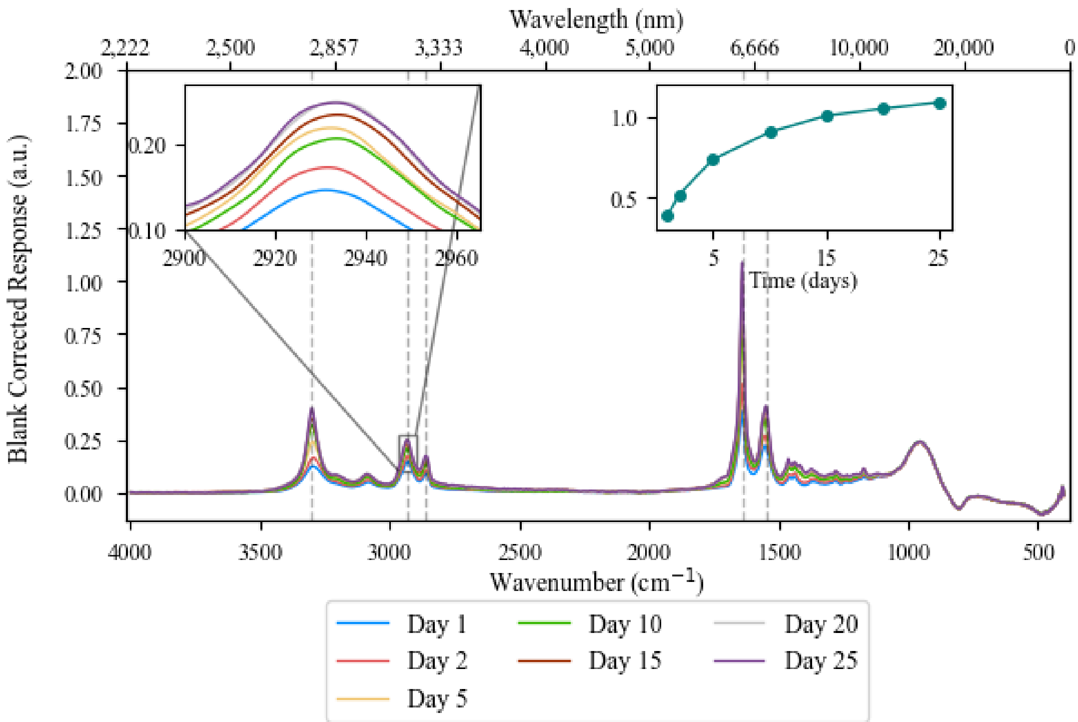

Figure 3.6: NEMS–FTIR spectra of aqueous extracts obtained from PA teabags, highlighting the C–H stretching region. The zoomed-in inset shows peak intensity evolution in the 2900–2970 cm^{-1} range.

3.3 PA Particles Samples

This section presents the spectral evolution of PA6 particle samples subjected to 25 days of artificial weathering. The results are based on NEMS–FTIR analysis of aqueous extracts and reveal progressive spectral changes across key vibrational regions, indicative of polymer oxidation and structural modification. The results are presented using five figures, including an overview spectrum of all time points, three detailed plots focusing on critical spectral regions, and a final comparison between Day 1 and Day 25.

Figure 3.7 shows an overview of the spectra across the mid-infrared region. Key changes are observed in the N–H stretching region (3300 cm^{-1}), the amide I and II regions (1650 and 1550 cm^{-1}), and the CH_2 stretching region (2930 cm^{-1}). These bands are known to be sensitive to degradation processes in polyamide materials [99, 102]. A similar pattern of spectral evolution was observed in the PA teabag samples, as shown in the previous section, with progressive intensity increases in the same vibrational regions, although the magnitude and consistency of the changes vary slightly between the two sample types.

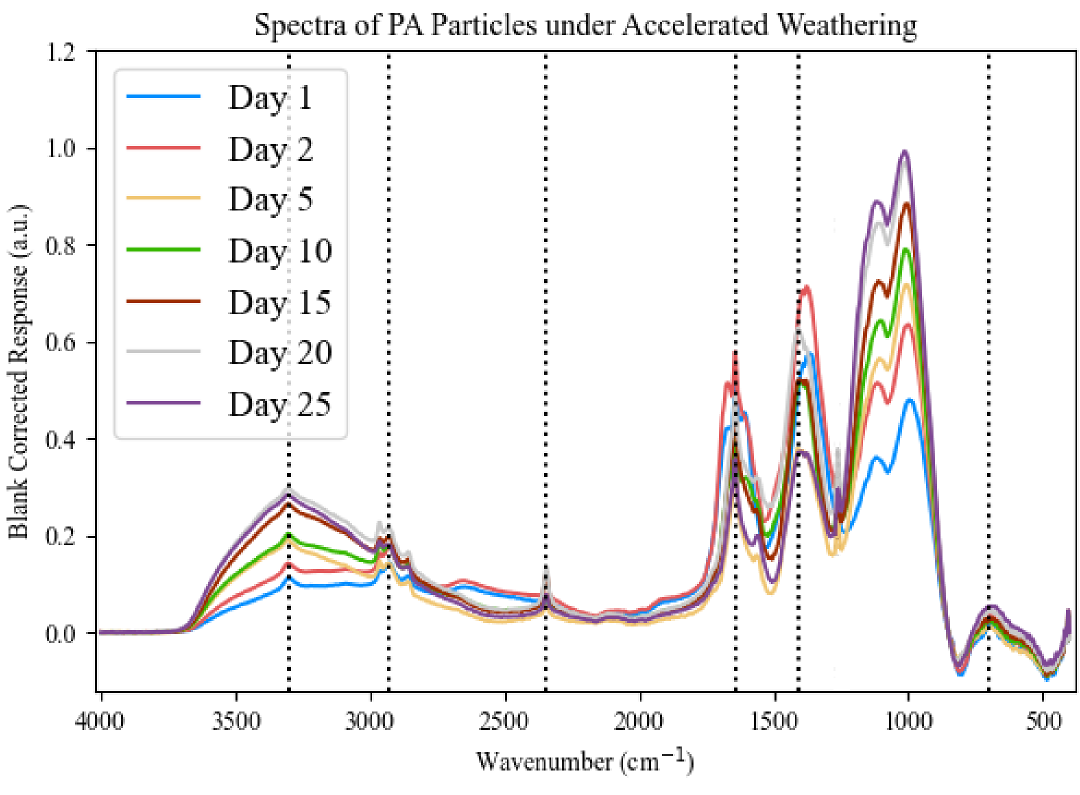

Figure 3.7: NEMS–FTIR spectra of aqueous extracts obtained from PA particles during 25 days of artificial weathering.

As shown in Figure 3.8, the N–H stretching band increases in intensity over time, consistent with enhanced hydrogen bonding due to oxidative surface modification and moisture uptake [103, 104]. In the amide I region (Figure 3.9), the band at 1650 cm^{-1} corresponds to C=O stretching vibrations in polyamide structures [99]. While this band has previously been associated with oxidation and structural changes in aged PA6 materials [101], a decrease in its intensity over time has also been reported under thermal oxidative aging conditions [103]. The spectra for PA particles in this study similarly show a gradual decline in the 1650 cm^{-1} band, suggesting a loss of ordered amide structures or changes in hydrogen bonding. This trend differs from the behavior observed in the PA teabag samples, where the amide I band increased over time, indicating a sample-dependent degradation response.

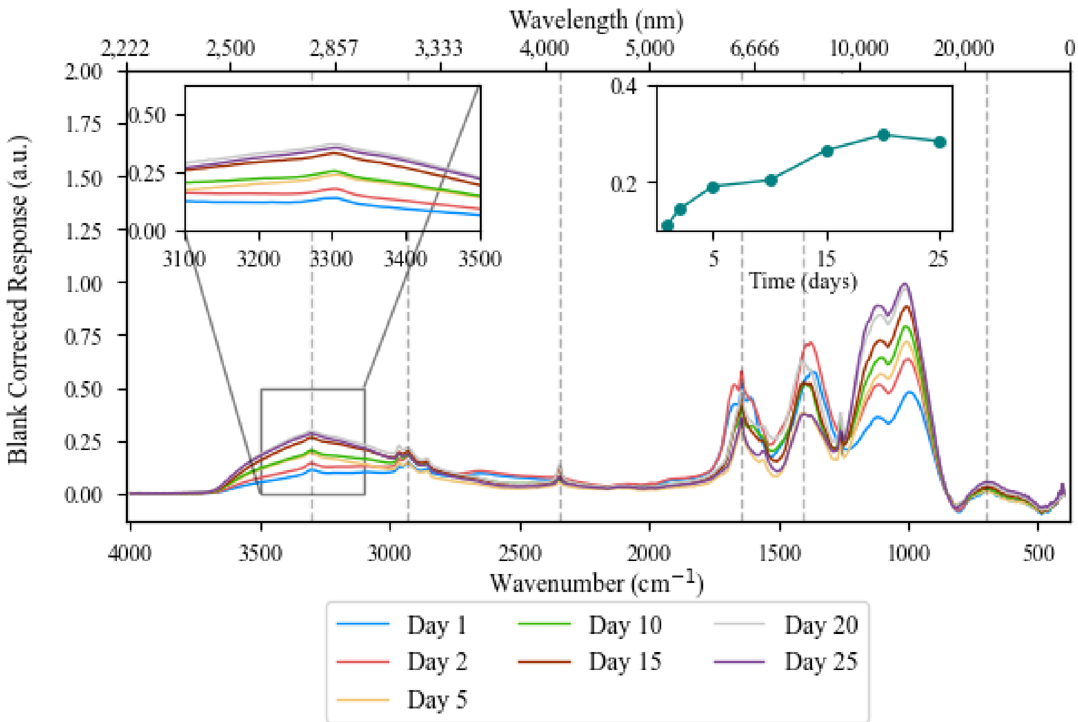

Figure 3.8: NEMS–FTIR spectra of aqueous extracts obtained from PA particles, highlighting the N–H stretching region. The zoomed-in inset shows the evolution of peak intensity in the 3100–3500 cm^{-1} range during artificial weathering.

To highlight the cumulative changes resulting from artificial weathering, Figure 3.10 presents a direct comparison of NEMS–FTIR spectra for PA particles on Day 1 and Day 25. Several characteristic vibrational bands show clear differences, including the broad N–H stretching region (3100–3500 cm^{-1}), the amide I region (1650 cm^{-1}), and the amide II region (1550 cm^{-1}).

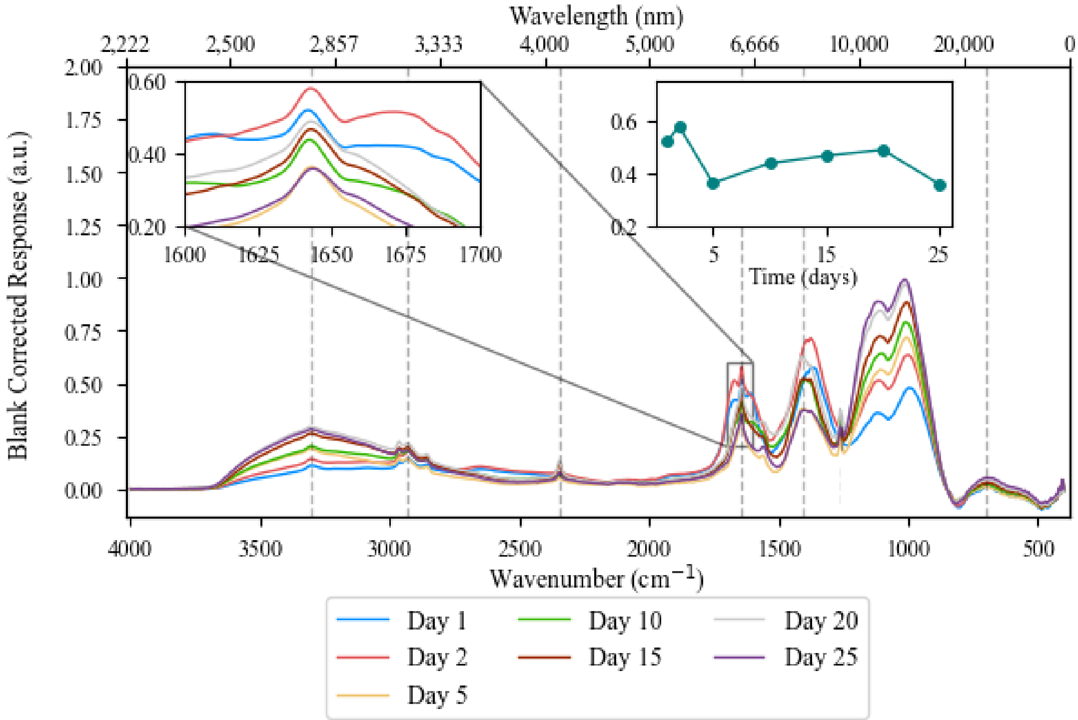

Figure 3.9: NEMS–FTIR spectra of aqueous extracts obtained from PA particles, highlighting the amide I region. The zoomed-in inset shows the evolution of peak intensity in the 1600–1700cm^{-1} range over 25 days of artificial weathering.

Compared to Day 1, the Day 25 spectrum exhibits an increased peak intensity near 3300 cm^{-1}, consistent with enhanced hydrogen bonding due to oxidative surface modification and moisture uptake [103, 104]. In contrast, the amide I and II bands show reduced intensity, a trend that has been previously reported during thermal oxidative degradation of PA6 [103]. This decrease has been linked to the loss of hydrogen-bonded amide structures and reduced molecular order in aged polyamides. Together, these changes reflect ongoing chemical and structural modification in PA materials under artificial weathering conditions, in agreement with prior observations of environmental and accelerated aging [104].

In summary, the NEMS–FTIR analysis of PA particles exposed to artificial weathering reveals progressive chemical and structural transformations over the 25-day period. Key spectral changes include increased O–H/N–H stretching due to hydroxyl formation, as well as attenuation of the amide I and II bands, indicating backbone degradation and reduced crystallinity. These results are consistent with previously reported degradation pathways in polyamide materials and confirm the susceptibility of PA to oxidative and hydrolytic breakdown under environmental stress.

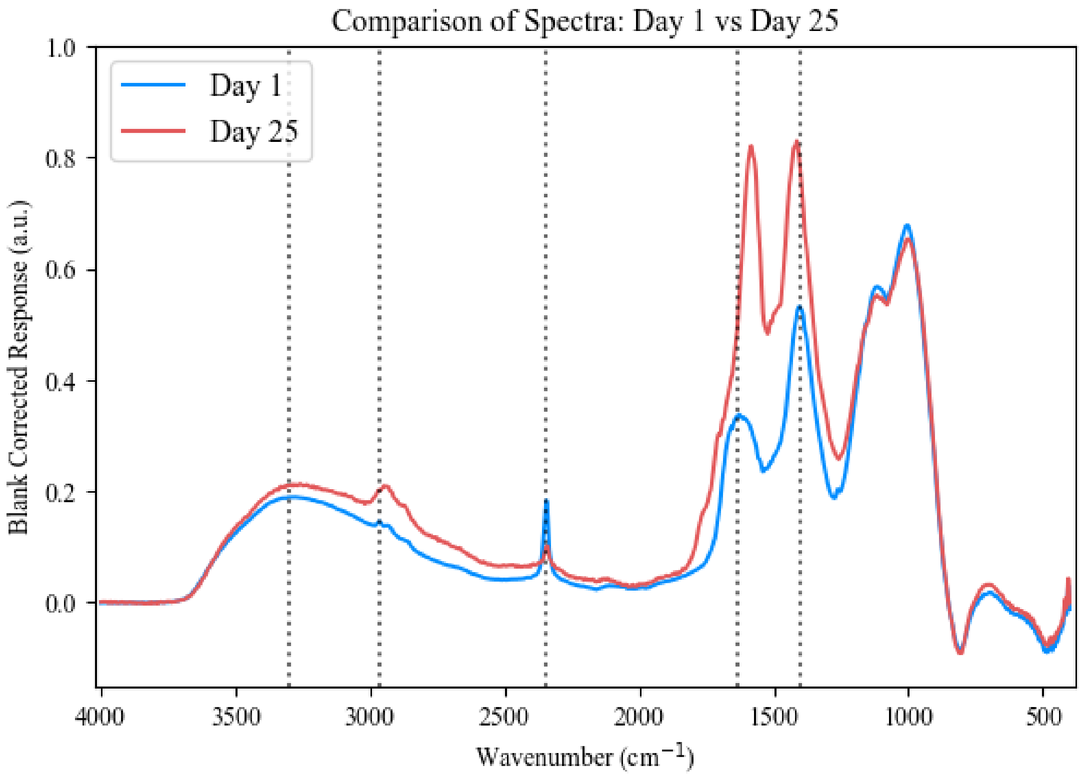

Figure 3.10: Comparison of NEMS–FTIR spectra of aqueous extracts obtained from PA particles on Day1 and Day25.

In summary, the NEMS–FTIR results for PA particles show increased N–H stretching and decreased amide I and II band intensities, indicating progressive chemical changes consistent with oxidative aging [99, 103, 104].

3.4 PS Lid Samples

This section examines the spectral changes observed in the aqueous extracts obtained from PS lids soaked in water and exposed to accelerated weathering over 25 days. The analysis is based on NEMS–FTIR measurements and interpreted in relation to established FTIR degradation patterns of polystyrene as reported by Campanale et al. [106], Lambert and Wagner [44], Yousif and Haddad [27], and Borgmeyer et al. [107]. The results are presented using five figures, including an overview spectrum of all time points and four detailed plots focusing on critical spectral regions.

Figure 3.11 presents the full spectral evolution. The key vibrational bands characteristic of pristine polystyrene—such as aromatic C–H stretching (3025–3080 cm^{-1}), aromatic C=C stretching (1600 and 1492 cm^{-1}), and out-of-plane C–H bending (755 and 698 cm^{-1})—remain detectable throughout the exposure period, indicating preservation of the aromatic backbone [106, 108].

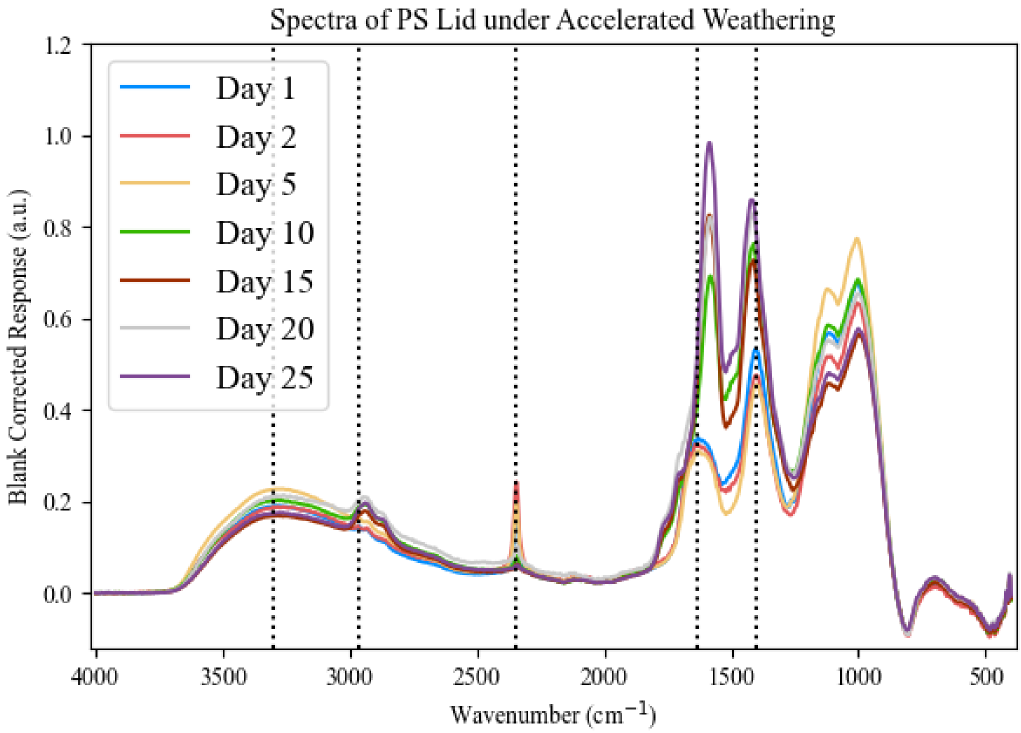

Figure 3.11: NEMS–FTIR spectra of aqueous extracts obtained from PS lids immersed in water over 25 days of accelerated weathering.

Figure 3.12 shows the evolution of the FTIR spectra in the 1500–1650cm^{-1} region for PS lid samples subjected to 25 days of artificial weathering. This region includes the aromatic C=C stretching mode typically centered near 1600cm^{-1}, which is a prominent feature of polystyrene [106, 108].

The figure reveals a gradual increase in peak intensity in this region over time, particularly between Day10 and Day25. This trend might indicate that the structure of the aromatic ring is retained during degradation but can become increasingly IR active due to local chemical modifications [106]. Such changes are consistent with early oxidative processes, where partial functionalization of the aromatic backbone occurs without complete cleavage of the ring [27].

The preservation and amplification of this band, also reported by Campanale et al. [106]

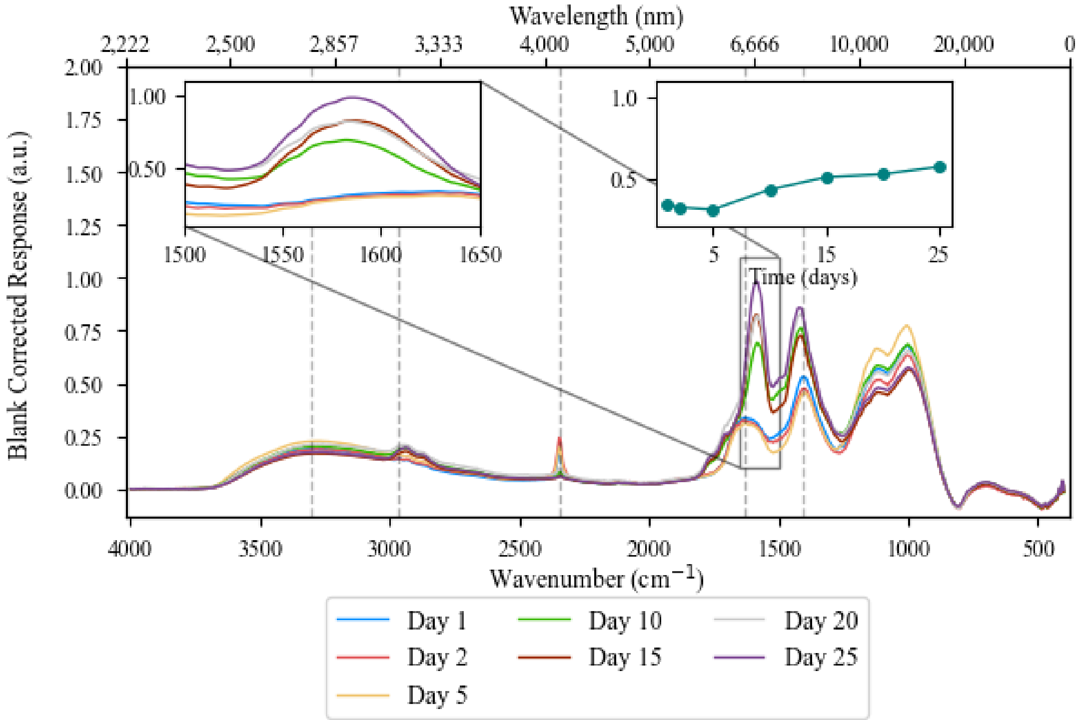

Figure 3.12: NEMS–FTIR spectra of aqueous extracts obtained from PS lids, highlighting the aromatic C=C stretching region. The zoomed-in inset shows peak intensity evolution in the 1500–1650 cm^{-1} range under accelerated weathering

in artificially aged PS fragments, suggest surface-level modification of the polystyrene matrix rather than bulk structural breakdown. This interpretation is further supported by Lambert and Wagner [44], who observed nanoplastic formation and surface erosion in PS lids without full aromatic degradation.

Figure 3.13 highlights the evolution of the 1350–1500cm^{-1} region in PS lid samples during 25 days of artificial weathering. This region contains key vibrational modes associated with polystyrene, including aromatic C–H bending and C=C stretching near 1450 and 1492cm^{-1} [106, 108].

The observed increase in peak intensity over time suggests the formation of new or modified vibrational environments within the polymer matrix. This may result from oxidative functionalization of the aromatic ring or local changes in the backbone symmetry, as has been previously reported during UV-induced degradation of PS [27, 106]. Campanale et al. noted similar growth in this region in aged PS fragments, linking it to increased ring substitution and environmental weathering effects.

Although no new peaks appear, the intensity amplification without shift implies that

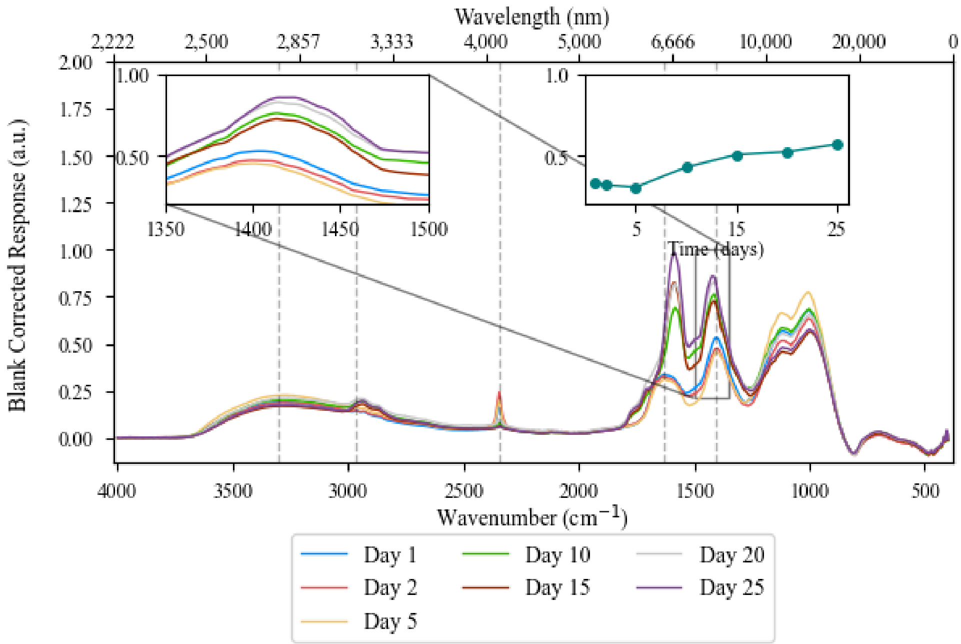

Figure 3.13: NEMS–FTIR spectra of aqueous extracts obtained from PS lids highlighting the C–H bending region. The inset shows the evolution of peak intensity in the 1350–1500 cm^{-1} range over the 25-day weathering period.

the phenyl rings are preserved but chemically modified. This is consistent with early-stage photooxidation, where side-group chemistry evolves while the core structure of PS remains intact [27, 107].

Figure 3.14 shows the FTIR spectra of aqueous extracts obtained from PS lids over a 25-day artificial weathering period, with a zoomed-in inset highlighting the 2300–2400cm^{-1} region. A sharp peak centered at 2344cm^{-1} is present across all time points. This band is not associated with polystyrene degradation products.

The 2344cm^{-1} signal is commonly attributed to the asymmetric stretching vibration of carbon dioxide (CO_2) [109]. It is well known in FTIR analysis that such peaks may arise from ambient atmospheric CO_2 or CO_2 adsorbed onto the sample or extract surface, especially when spectra are acquired without full gas purging. The persistence and narrowness of this peak suggest it originates from external sources rather than chemical transformations in the PS matrix.

Accordingly, the feature at 2344 cm^{-1} is interpreted as a non-informative artifact and is not considered evidence of PS degradation in the aqueous extracts.

Figure 3.15 focuses on the 3200–3400cm^{-1} region in the FTIR spectra of aqueous extracts

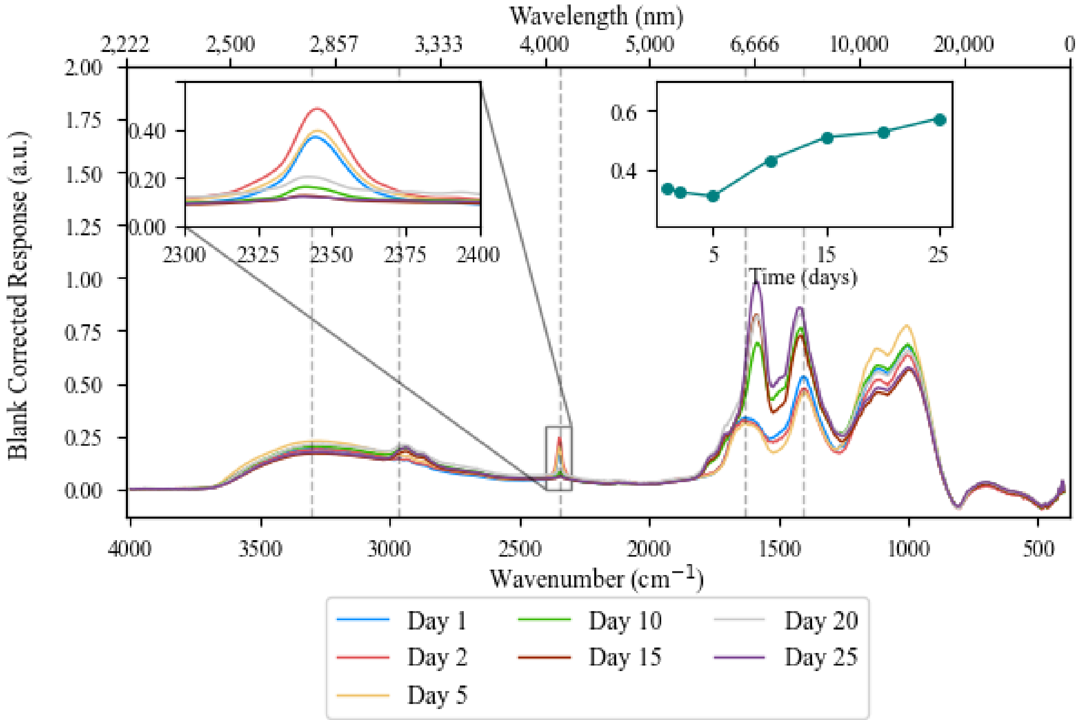

Figure 3.14: NEMS–FTIR spectra of aqueous extracts obtained from PS lids, highlighting the CO_2 band. The zoomed-in inset shows the spectral evolution in the 2300–2400 cm^{-1} range over the course of 25 days of accelerated weathering.

obtained from PS lids during 25 days of artificial weathering. This broad region is commonly attributed to O–H stretching vibrations, associated with hydroxyl-containing species such as alcohols, carboxylic acids, or adsorbed water [27, 106].

The gradual increase in intensity over time suggests the formation of hydroxylated surface groups as a result of oxidative degradation [106].

This trend is consistent with prior studies that observed UV-induced oxidation of polystyrene leading to hydroxyl group incorporation, particularly on the polymer surface [107].

Although the band remains broad and lacks fine structure, its progression over time might suggest surface-level chemical transformation, likely driven by oxygen and moisture exposure during the weathering process.

Spectral analysis of aqueous extracts obtained from PS lids demonstrated that several vibrational regions, including those associated with aromatic C=C stretching, aliphatic C-H, and hydroxyl groups, undergo a gradual increase in intensity during the 25-day artificial weathering period. In particular, these changes begin to emerge clearly after Day5, aligning

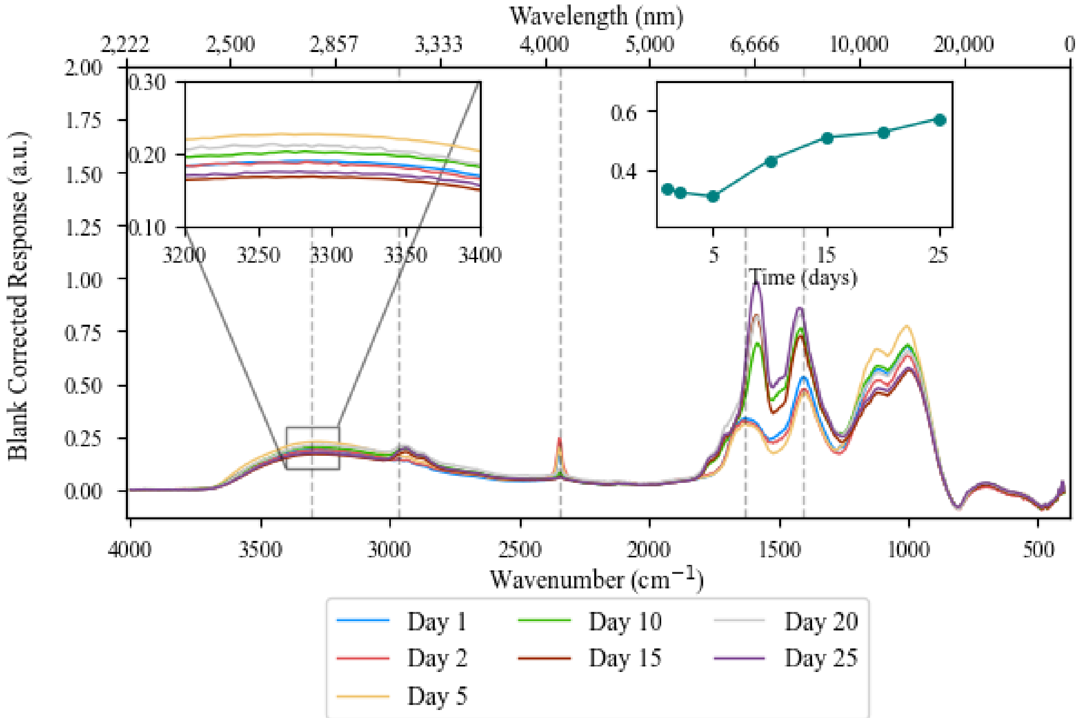

Figure 3.15: NEMS–FTIR spectra of aqueous extracts obtained from PS lids, highlighting the O–H stretching region. The zoomed-in inset shows peak intensity evolution in the 3200–3400 cm^{-1} range.

with the onset of observable physical degradation in the samples. As shown in Figure3.1(a), PS lid fragments developed visible yellowing and became increasingly brittle after Day 5. This correlation between spectral evolution and macroscopic deterioration reinforces the conclusion that surface-level chemical modifications, particularly oxidative degradation, are responsible for the early stages of material breakdown in PS lids under environmental stress.

The following section focuses on PS particles to evaluate whether similar degradation patterns occur at the nanoscale and to what extent particle size and surface area influence the spectroscopic response.

3.5 PS Particles Samples

The NEMS–FTIR spectra of aqueous extracts from PS particles subjected to accelerated weathering over 25 days exhibit evident changes in multiple vibrational regions. Due to variability in peak progression across intermediate time points, the analysis focuses on comparative evaluation between Day1, Day25, and a pristine PS reference. Specific spectral regions are highlighted to provide insight into chemical changes related to oxidative degradation and structural modification.

Figure 3.16 shows the full NEMS–FTIR spectral evolution of aqueous extracts from PS particles over a 25-day artificial weathering period. Across the spectrum, key vibrational features associated with polystyrene are preserved, including the aromatic C–H stretching bands (3025–3080cm^{-1}), the aromatic C=C stretching bands (1600 and 1492cm^{-1}), and the strong fingerprint bands near 755 and 698cm^{-1} [106, 108].

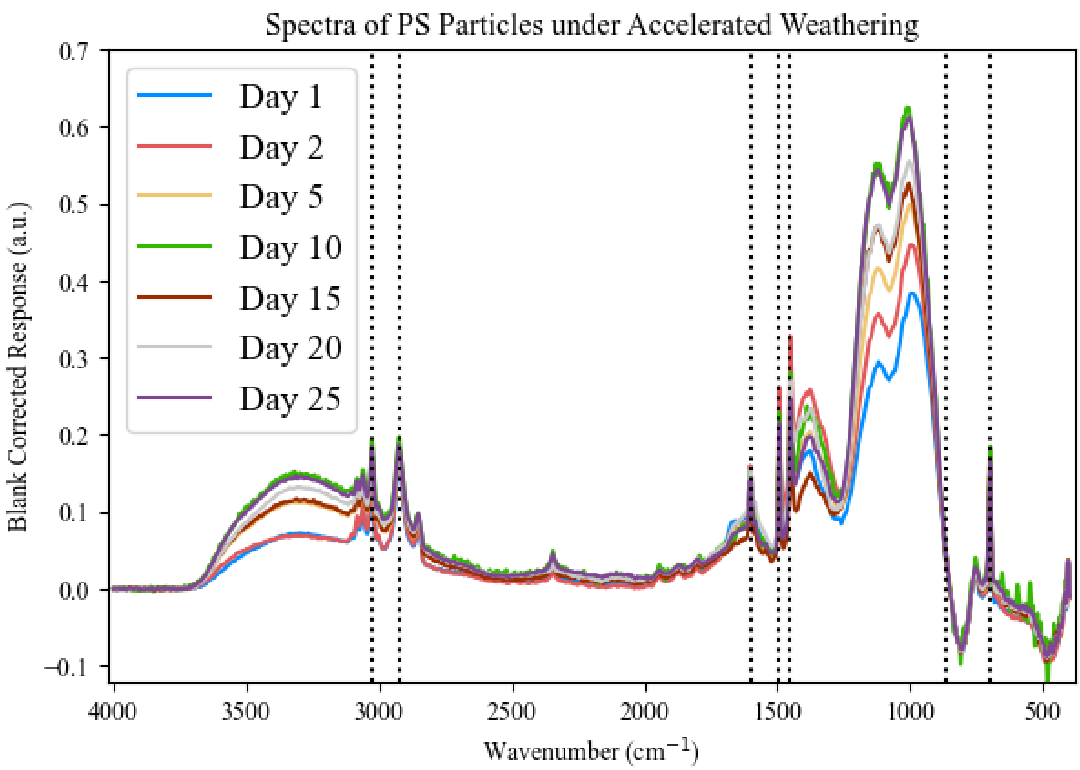

Figure 3.16: NEMS–FTIR spectra of aqueous extracts obtained from PS particles subjected to accelerated weathering over 25 days.

Although overall spectral changes were observed throughout the weathering period, the evolution of peak intensities was not strictly linear. In most regions, the highest intensities were recorded around Day10, followed by a slight decline or stabilization at later time points. As this trend was not reported in comparable FTIR studies on PS degradation [106, 107], it may reflect variability introduced by sampling conditions, such as differences in particle distribution, extract concentration, or surface contact during measurement. These effects are particularly relevant in analyses involving aqueous extracts from heterogeneous particulate materials.

Figure 3.17 presents a comparison of NEMS–FTIR spectra of aqueous extracts obtained from PS particles on Day 1, Day 25, and an unweathered reference sample (10 ng). The reference spectrum exhibits only the characteristic aromatic and aliphatic PS bands with minimal background, confirming its chemical stability. In contrast, both aged samples display higher peaks across several regions, particularly Day25, which shows elevated signals in the O–H stretching (3200–3500cm^{-1}) and fingerprint (600–1500cm^{-1}) regions. These changes are consistent with oxidation-related surface modifications reported in literature [106, 107].

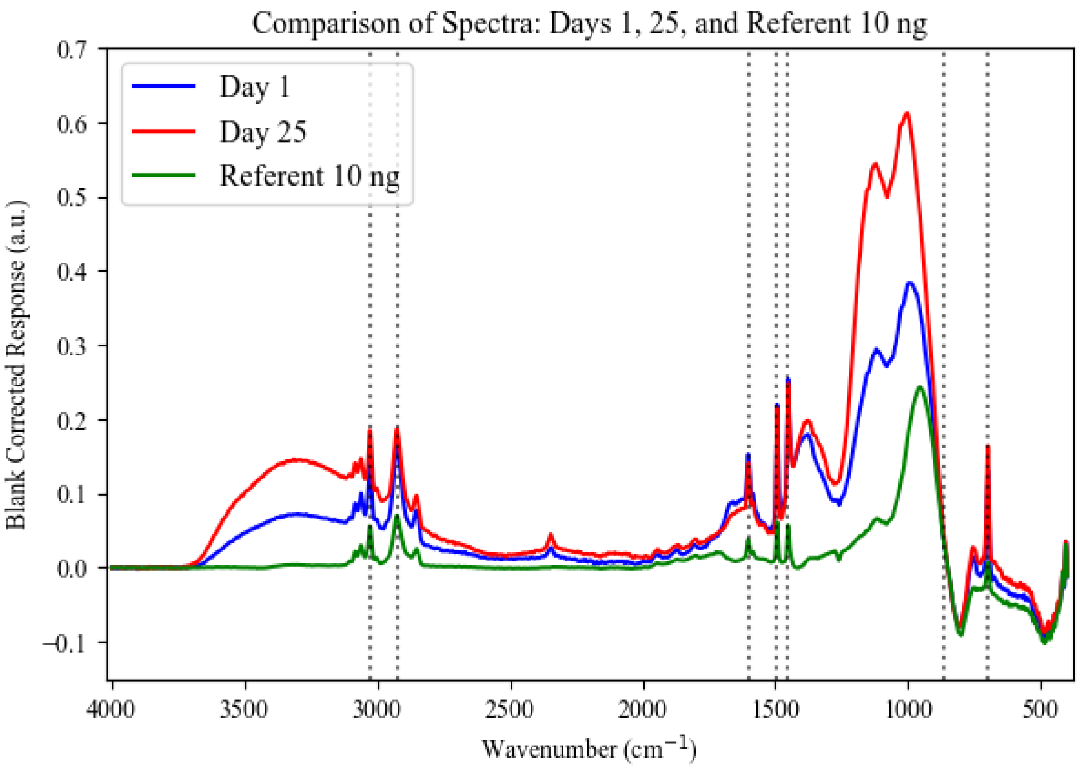

Figure 3.17: Comparison of NEMS–FTIR spectra of aqueous extracts obtained from PS particles on Day1, Day25, and an unweathered reference sample (10 ng).

Figure 3.18 presents NEMS–FTIR spectra of aqueous extracts obtained from PS particles, highlighting the fingerprint region (600–1500 cm^{-1}) for Day 1, Day 25, and a pristine 10 ng reference sample. The Day25 spectrum shows the highest peak intensities across multiple bands, particularly near 1000–1100cm^{-1} and 750–700cm^{-1}, which are attributed to ring bending and out-of-plane C–H vibrations characteristic of polystyrene [106, 108]. The overall increase in peak intensity in this region suggests progressive accumulation of surface oxidation products and enhanced IR activity due to chemical modifications induced by weathering.

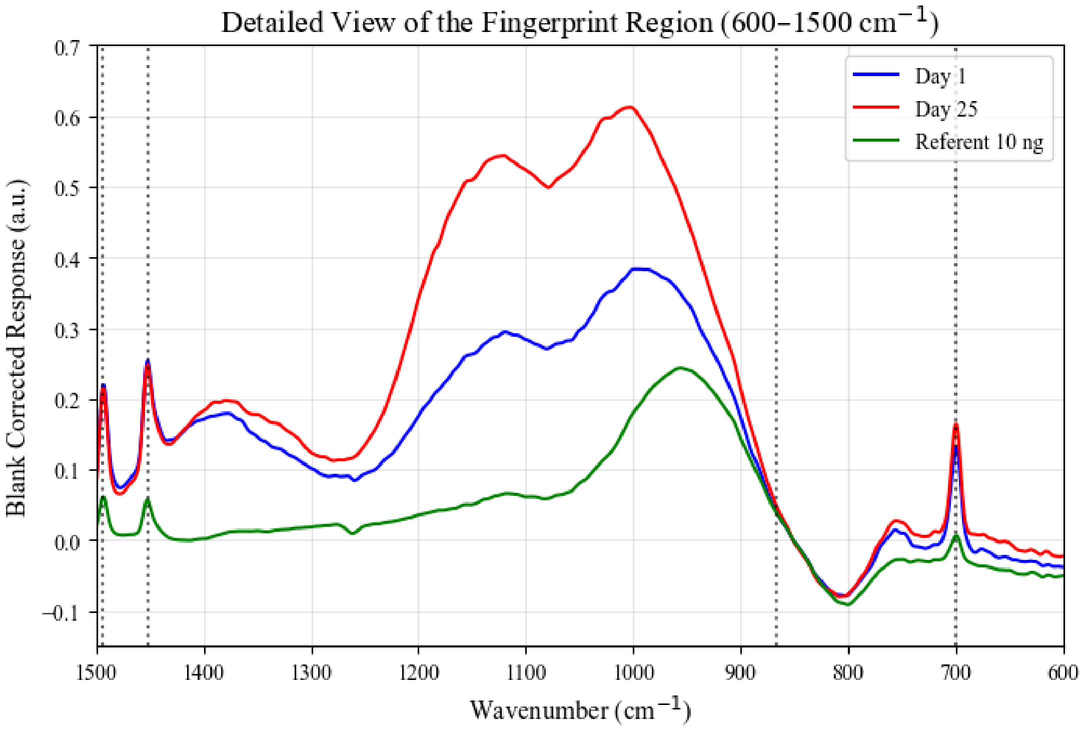

Figure 3.18: NEMS–FTIR spectra of aqueous extracts obtained from PS particles, detailed view the fingerprint region (600–1500 cm^{-1}).

Figure 3.19 shows a zoomed-in view of the aromatic C=C stretching band centered near 1495cm^{-1} in PS particle extracts. This band is a well-established diagnostic marker of the polystyrene aromatic backbone [106, 108]. It is clearly present in both Day1 and Day25 spectra, with Day 1 exhibiting slightly higher peak intensity. The reference sample displays a much lower response, consistent with its lower concentration. The overall preservation of this signal over time suggests that the core aromatic structure of the PS particles remains chemically stable throughout the aging process, despite surface-level oxidative modifications observed in other spectral regions.

Figure 3.20 shows the evolution of the O–H stretching region (3200–3500cm^{-1}) in the FTIR spectra of PS particle extracts. This broad absorption band is typically associated with

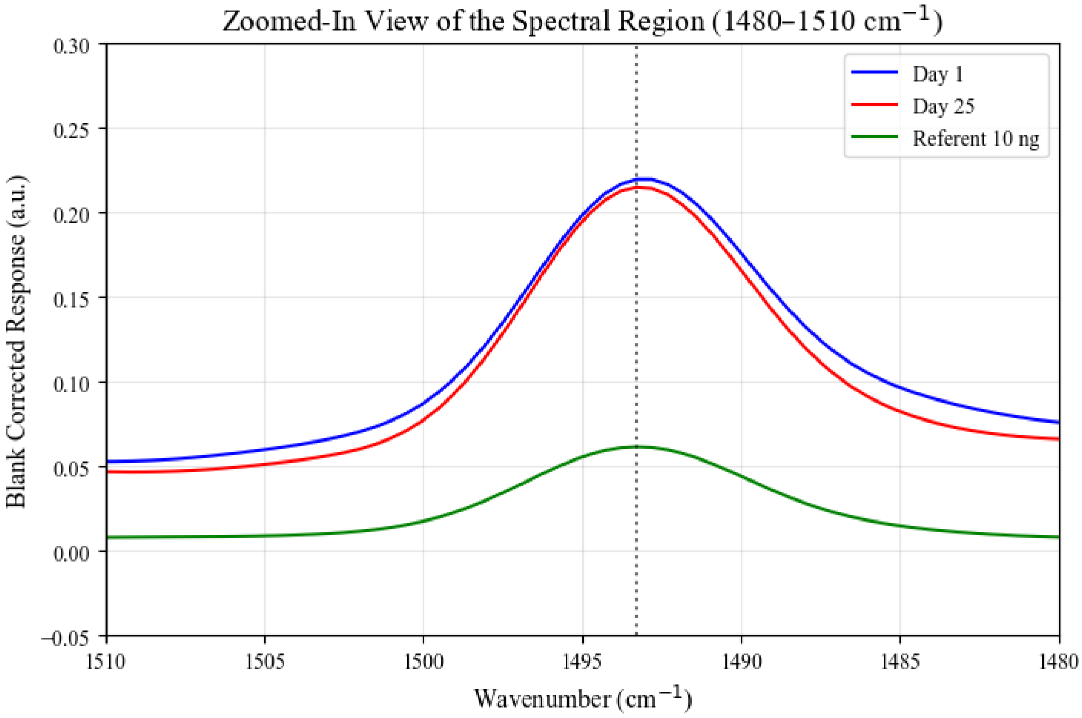

Figure 3.19: NEMS–FTIR spectra of aqueous extracts obtained from PS particles, highlighting the aromatic C=C stretching region. The zoomed-in inset shows spectral features in the 1480–1510 cm^{-1} range.

hydroxyl-containing species, including alcohols, carboxylic acids, or adsorbed water [106,107]. A clear increase in peak intensity is observed from Day1 to Day25, while the pristine PS reference shows minimal response. This trend is consistent with progressive surface oxidation and the formation of polar oxygen-containing groups on the PS particles during weathering.

In summary, the NEMS–FTIR analysis of aqueous extracts from polystyrene particles exposed to accelerated weathering revealed progressive surface modification characterized by increasing peak intensities in the O–H stretching region and key fingerprint bands. While core aromatic structures remained intact, the emergence of hydroxyl-related signals and enhanced activity in degradation-sensitive regions suggest oxidative transformation at the particle surface. These findings align with previously reported weathering behavior in polystyrene materials [106, 107], and support the broader conclusion of Chapter 3, namely that FTIR spectroscopy enables detection of early-stage chemical degradation in polymer samples even without direct preconcentration or filtration steps.

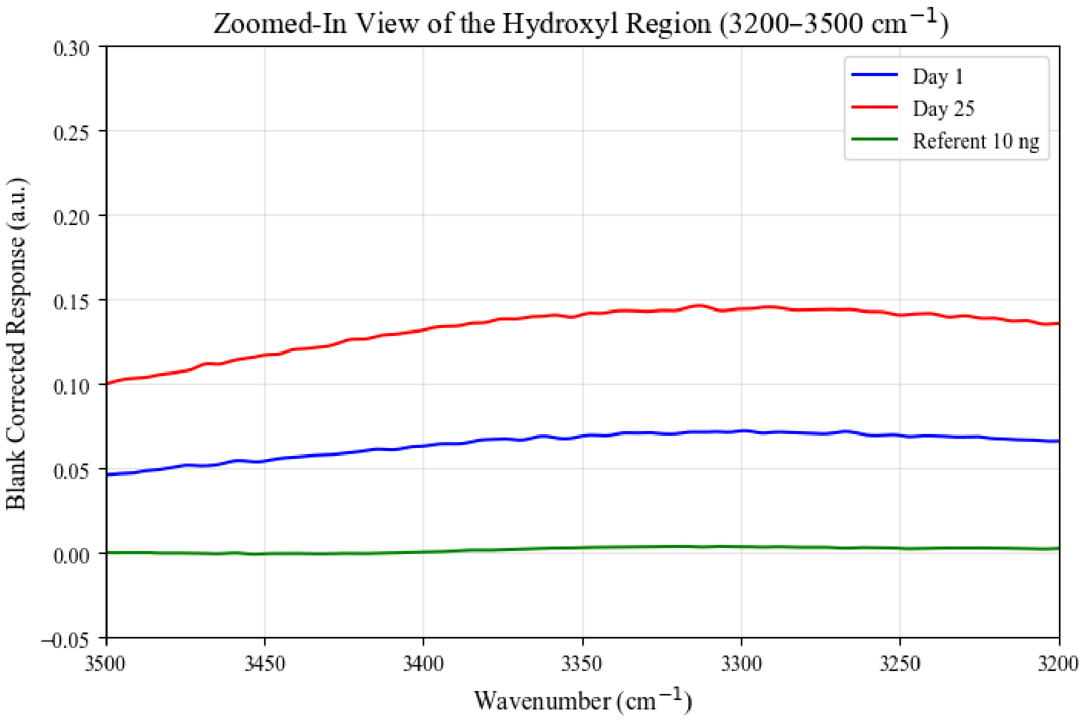

Figure 3.20: NEMS–FTIR spectra of aqueous extracts obtained from PS particles, highlighting the O–H stretching region. The zoomed-in inset shows increasing peak intensity in the 3200–3500 cm^{-1} range with weathering duration.

Chapter 4

Conclusion and Outlook

This thesis aimed to investigate the chemical and structural degradation of PA, PS, and PET materials under artificially induced weathering conditions, using NEMS-FTIR spectroscopy. To simulate environmental exposure, an accelerated weathering protocol was applied over 25 days, combining UV radiation and thermal cycling. The development of characteristic vibrational bands was tracked in two polymer types (PA and PS) over a 25-day exposure period. This included changes in O–H/N–H stretching (3100–3500 cm^{-1}), amide I and II bands (1600–1700 and 1500–1600 cm^{-1}), and aromatic and aliphatic C–H regions. The observed spectral changes indicated progressive oxidation, hydrolysis, and chain scission, consistent with degradation mechanisms reported in the literature. Although PET was initially included in the study, it was excluded from the final analysis due to weak spectral responses and limited degradation under the applied weathering conditions.

Macroscopic inspection and mass tracking complemented the spectroscopic analysis, allowing visual and quantitative observation of degradation effects in all three types of polymers. Notably, PS showed visible yellowing and embrittlement, while PA exhibited minor but measurable mass loss, supporting the chemical changes observed spectroscopically.

This work has also shown the practical strength of NEMS-FTIR as a detection tool. The key advantage of this method is the ability to identify plastic materials using minimal sample quantities, often without the need for pre-concentration. In contrast to earlier studies, which required steeping up to 60 teabags in 200 mL of water to detect nanoplastics [110, 111], NEMS-FTIR has been shown to detect PA particles from a single teabag in only 30 mL of water exposed to the aging process. This improvement demonstrates the method's high sensitivity and its applicability for detecting chemical changes in plastic degradation products in low-concentration aqueous samples, without the need for preconcentration.

Additionally, NEMS-FTIR overcomes the limitations of traditional FTIR or Raman microscopy by enabling the chemical identification of micro- and nanoplastics regardless of particle size. Its non-destructive nature allows seamless integration with complementary techniques such as SEM, EDX, and O-PTIR, facilitating multi-modal sample characterization. Crucially, the configuration is affordable and accessible for regular environmental monitoring due to the use of commercially available FTIR sources. Transparent and repeatable analytical methods are further supported by the use of open-source spectrum libraries such as Open Specy and Spectragryph.

In addition to this, compared to earlier nanoplastic degradation studies, such as Lambert and Wagner's investigation of PS breakdown using nanoparticle tracking analysis (NTA) [44], the NEMS-FTIR approach employed in this thesis offers significant advantages. While their study required up to 14 days to observe measurable nanoplastic formation and relied on size-based particle counting, NEMS-FTIR provided chemical information about degradation signatures, such as O–H stretching and amide bond evolution, within the first few days of exposure. Moreover, NEMS-FTIR allows for simultaneous chemical identification and monitoring of structural changes, which NTA cannot achieve. These differences underline the broader analytical power and faster diagnostic potential of NEMS-based spectroscopy in nanoplastics research.

Looking ahead, NEMS-based spectroscopy holds strong potential for nanoplastic detection in complex matrices such as air, soil, or biological fluids. Future developments may focus on improving automated sample handling, real-time spectral acquisition, and coupling with portable instruments. The findings of this thesis provide a foundational step in this direction, establishing NEMS-FTIR as a reliable and sensitive tool for detecting degradation in polymer materials and advancing the field of nanoscale plastic analysis.

Bibliography

[1] Y. Xue, K. Song, Z. Wang, Z. Xia, R. Li, Q. Wang, and L. Li. Nanoplastics occurrence, detection methods, and impact on the nitrogen cycle: a review. *Environmental Chemistry Letters*, 22(5):2241–2255, 2024.

[2] Matthew Cole, Pennie Lindeque, Claudia Halsband, and Tamara S. Galloway. Microplastics as contaminants in the marine environment: A review. *Marine Pollution Bulletin*, 62(12):2588–2597, 2011.

[3] Matthew Cole and Tamara S. Galloway. Ingestion of nanoplastics and microplastics by pacific oyster larvae. *Environmental Science & Technology*, 49(24):14625–14632, 2015. PMID: 26580574.

[4] Albert A. Koelmans, Ellen Besseling, and Edwin M. Foekema. Leaching of plastic additives to marine organisms. *Environmental Pollution*, 187:49–54, 2014.

[5] João Pinto da Costa, Patrícia S.M. Santos, Armando C. Duarte, and Teresa Rocha-Santos. (nano)plastics in the environment – sources, fates and effects. *Science of The Total Environment*, 566-567:15–26, 2016.

[6] I. O. Musa, H. S. Auta, U. S. Ilyasu, S. A. Aransiola, H. A. Makun, N. U. Adabara, O. P. Abioye, A. Aziz, B. Jayanthi, N. R. Maddela, and R. Prasad. Micro- and nanoplastics in environment: Degradation, detection, and ecological impact. *International Journal of Environmental Research*, 18(1):45–67, 2023.

[7] S. Adhikari, V. Kelkar, R. Kumar, and R. U. Halden. Methods and challenges in the detection of microplastics and nanoplastics: a mini-review. *Polymer International*, 71(5):543–551, 2022.

[8] C. Zangmeister, J. Radney, K. Benkstein, and B. Kalanyan. Common single-use consumer plastic products release trillions of sub-100 nm nanoparticles per liter into water during normal use. *Environmental Science and Technology*, 56(4):2233–2241, 2022.

[9] J. Caldwell, P. Taladriz-Blanco, R. Lehner, A. Lubskyy, R. D. Ortuso, B. Rothen-Rutishauser, and A. Petri-Fink. The micro-, submicron-, and nanoplastic hunt: A review of detection methods for plastic particles. *Chemosphere*, 293:133514, 2022.

[10] L. Tian, E. Skoczynska, R.-J. van Putten, H. A. Leslie, and G.-J. M. Gruter. Quantification of polyethylene terephthalate micro- and nanoplastics in domestic wastewater using a simple three-step method. *Science of The Total Environment*, 857:159209, 2023.

[11] W. Zhang, Q. Wang, and H. Chen. Challenges in characterization of nanoplastics in the environment. *Frontiers of Environmental Science & Engineering*, 16(1):11, 2022.

[12] N. Bikiaris, N. F. Nikolaidis, and P. Barmpalexis. Microplastics (mps) in cosmetics: A review on their presence in personal-care, cosmetic, and cleaning products (pccps) and sustainable alternatives from biobased and biodegradable polymers. *Cosmetics*, 11(5):145, 2024.

[13] H. A. Leslie, M. J. M. van Velzen, S. H. Brandsma, A. D. Vethaak, J. J. Garcia-Vallejo, and M. H. Lamoree. Discovery and quantification of plastic particle pollution in human blood. *Environment International*, 163:107199, 2022.

[14] Q. Zhao, L. Zhu, J. Weng, Z. Jin, Y. Cao, H. Jiang, and Z. Zhang. Detection and characterization of microplastics in the human testis and semen. *Science of The Total Environment*, 877:162713, 2023.

[15] E. Zettler, T. Mincer, and L. Amaral-Zettler. Life in the "plastisphere": Microbial communities on plastic marine debris. *Environmental Science & Technology*, 47(13):7137–7146, 2013.

[16] D. R. Osuna-Laveaga, V. Ojeda-Castillo, V. Flores-Payán, A. Gutiérrez-Becerra, and E. D. Moreno-Medrano. Micro- and nanoplastics current status: legislation, gaps, limitations and socio-economic prospects for future. *Frontiers in Environmental Science*, 11:1241939, 2023.

[17] C. Casella, D. Vadivel, and D. Dondi. The current situation of the legislative gap on microplastics (mps) as new pollutants for the environment. *Water, Air, and Soil Pollution*, 235:778, 2024.

[18] A. Käppler, D. Fischer, S. Oberbeckmann, G. Schernewski, M. Labrenz, K.-J. Eichhorn, and B. Voit. Analysis of environmental microplastics by vibrational microspectroscopy: Ftir, raman, or both? *Analytical and Bioanalytical Chemistry*, 408(31):8377–8391, 2016.

[19] Xiao-Xia Zhou, Rui Liu, Li-Teng Hao, and Jing-Fu Liu. Identification of polystyrene nanoplastics using surface enhanced raman spectroscopy. *Talanta*, 221:121552, 2021.

[20] Rui Hu, Kaining Zhang, Wei Wang, Long Wei, and Yongchao Lai. Quantitative and sensitive analysis of polystyrene nanoplastics down to 50 nm by surface-enhanced raman spectroscopy in water. *Journal of Hazardous Materials*, 429:128388, 2022.

[21] Elvis D. Okoffo and Kevin V. Thomas. Quantitative analysis of nanoplastics in environmental and potable waters by pyrolysis-gas chromatography–mass spectrometry. *Journal of Hazardous Materials*, 464:133013, 2024.

[22] Haiyan Li, Lin Min Lee, Dingyi Yu, Sheot Harn Chan, and Angela Li. An optimized multi-technique based analytical platform for identification, characterization and quantification of nanoplastics in water. *Talanta*, 272:125800, 2024.

[23] Robert G. West, Kostas Kanellopulos, and Silvan Schmid. Photothermal microscopy and spectroscopy with nanomechanical resonators. *The Journal of Physical Chemistry C*, 127(45):21915–21929, 2023.

[24] Niklas Luhmann, Robert G. West, Josiane P. Lafleur, and Silvan Schmid. Nanoelectromechanical infrared spectroscopy with in situ separation by thermal desorption: Nems-ir-td. *ACS Sensors*, 8(4):1462–1470, 2023. PMID: 37067504.

[25] ST Rabie, AM Mahran, EM Kamel, and NH Abdel Hamid. Photodegradation of polystyrene stabilized with uracil derivative. *Journal of applied sciences research*, 4(12):2015–2026, 2008. [Online]. Available: https://www.researchgate.net/publication/280102340.

[26] G. Geuskens and C. David. *Degradation and Stabilization of Polymers*. Halsted, Wiley, New York, 1975.

[27] Emad Yousif and Raghad Haddad. Photodegradation and photostabilization of polymers, especially polystyrene: review. *SpringerPlus*, 2(1):398, 2013.

[28] Anthony L. Andrady. Microplastics in the marine environment. *Marine Pollution Bulletin*, 62(8):1596–1605, 2011.

[29] Berit Gewert, Merle M. Plassmann, and Matthew MacLeod. Pathways for degradation of plastic polymers floating in the marine environment. *Environmental Science: Processes & Impacts*, 17(9):1513–1521, 2015.

[30] Polystyrene. Wikipedia. Oct. 17, 2024. Accessed: Nov. 1, 2024. [Online]. Available: https://en.wikipedia.org/wiki/Polystyrene.

[31] Richard C. Thompson, Shanna H. Swan, Charles J. Moore, and Frederick S. vom Saal. Our plastic age. *Philosophical Transactions of the Royal Society B: Biological Sciences*, 364(1526):1973–1976, 2009.

[32] M. Rochman, C. A. Browne, M. S. Halpern, B. et al. Classify plastic waste as hazardous. *Nature*, 494:169–171, 2013.

[33] Bum Gun Kwon, Katsuhiko Saido, Koshiro Koizumi, Hideto Sato, Naoto Ogawa, Seon Yong Chung, Takashi Kusui, Yoichi Kodera, and Kazuhio Kogure. Regional distribution of styrene analogues generated from polystyrene degradation along the

coastlines of the north-east pacific ocean and hawaii. *Environmental Pollution*, 188:45–49, 2014.

[34] Sophia Opperskalski, S Siew, Evonne Tan, and Liesl Truscott. Preferred fiber & materials market report 2019. *Textile Exchange: Lamesa, TX, USA*, 2019.

[35] Valter Castelvetro, Andrea Corti, Alessio Ceccarini, Antonella Petri, and Virginia Vinciguerra. Nylon 6 and nylon 6,6 micro- and nanoplastics: A first example of their accurate quantification, along with polyester (pet), in wastewater treatment plant sludges. *Journal of Hazardous Materials*, 407:124364, 2021.

[36] P. K. Vagholkar. Nylon (chemistry, properties and uses). *International Journal of Scientific Research*, 5:349–351, 09 2016.

[37] Nylon 6. Wikipedia. Oct. 30, 2024. Accessed: Nov. 1, 2024. [Online]. Available: https://en.wikipedia.org/wiki/Nylon_6.

[38] World Economic Forum, Ellen MacArthur Foundation, and McKinsey & Company. The new plastics economy: Rethinking the future of plastics, 2016.

[39] Tian Sang, Christopher J. Wallis, Gavin Hill, and George J.P. Britovsek. Polyethylene terephthalate degradation under natural and accelerated weathering conditions. *European Polymer Journal*, 136:109873, 2020.

[40] V. Sinha, R. Patel, M. and V. Patel, J.˙Pet waste management by chemical recycling: A review. *Journal of Polymers and the Environment*, 18(1):8–25, 2010.

[41] Polyethylenterephthalat. Wikipedia. Sep. 4, 2024. Accessed: Nov. 1, 2024. [Online]. Available: https://de.wikipedia.org/wiki/Polyethylenterephthalat.

[42] Tangram Technology Ltd. Weathering of plastics. [Online]. Available: http://www.tangram.co.uk/.

[43] James E. Pickett. Chapter 8 - weathering of plastics. In Myer Kutz, editor, *Handbook of Environmental Degradation of Materials (Third Edition)*, pages 163–184. William Andrew Publishing, third edition edition, 2018.

[44] Scott Lambert and Martin Wagner. Characterisation of nanoplastics during the degradation of polystyrene. *Chemosphere*, 145:265–268, 2016.

[45] Nora Meides, Teresa Menzel, Björn Poetzschner, Martin G. J. Löder, Ulrich Mansfeld, Peter Strohriegl, Volker Altstaedt, and Jürgen Senker. Reconstructing the environmental degradation of polystyrene by accelerated weathering. *Environmental Science & Technology*, 55(12):7930–7938, 2021.

[46] Teresa Menzel, Nora Meides, Anika Mauel, Ulrich Mansfeld, Winfried Kretschmer, Meike Kuhn, Eva M. Herzig, Volker Altstädt, Peter Strohriegl, Jürgen Senker, and Holger Ruckdäschel. Degradation of low-density polyethylene to nanoplastic particles by accelerated weathering. *Science of The Total Environment*, 826:154035, 2022.

[47] A. Gok, C. L. Fagerholm, D. A. Gordon, L. S. Bruckman, and R. H. French. Degradation of poly(ethylene-terephthalate) under accelerated weathering exposures. In *2015 IEEE 42nd Photovoltaic Specialist Conference (PVSC)*, pages 1–6, 2015.

[48] M. Philip and F. Al-Azzawi. Effects of natural and artificial weathering on the physical properties of recycled poly(ethylene terephthalate). *Journal of Polymers and the Environment*, 26(8):3139–3148, 2018.

[49] ASTM International. Astm d4329-13: Standard practice for fluorescent ultraviolet (uv) lamp apparatus exposure of plastics, 2013. [Online]. Available: https://www.astm.org/d4329.

[50] International Organization for Standardization. Iso 4892-3:2016: Plastics — methods of exposure to laboratory light sources — part 3: Fluorescent uv lamps, 2016. [Online]. Available: https://www.iso.org/standard/67852.html.

[51] ASTM International. Astm g154-16: Standard practice for operating fluorescent ultraviolet (uv) lamp apparatus for exposure of nonmetallic materials, 2016. [Online]. Available: https://www.astm.org/g0154.

[52] International Organization for Standardization. Iso 4892-2:2013: Plastics — methods of exposure to laboratory light sources — part 2: Xenon-arc lamps, 2013. [Online]. Available: https://www.iso.org/standard/56462.html.

[53] ASTM International. Astm g155-13: Standard practice for operating xenon arc light apparatus for exposure of non-metallic materials, 2013. [Online]. Available: https://www.astm.org/g0155.

[54] J. Andrade, V. Fernández-González, P. López-Mahía, and S. Muniategui. A low-cost system to simulate environmental microplastic weathering. *Marine Pollution Bulletin*, 149:110663, 2019.

[55] S. Lambert and M. Wagner. Formation of microscopic particles during the degradation of different polymers. *Chemosphere*, 161:510–517, 2016.

[56] S.M. Al-Salem. Influence of natural and accelerated weathering on various formulations of linear low density polyethylene (lldpe) films. *Materials Design*, 30(5):1729–1736, 2009.

[57] J. H. Bridson, R. Abbel, D. A. Smith, G. L. Northcott, and S. Gaw. Impact of accelerated weathering on the leaching kinetics of stabiliser additives from microplastics. *Journal of Hazardous Materials*, 459:132303, 2023.

[58] L. Wei, X. Kuai, Y. Bao, J. Wei, L. Yang, P. Song, M. Zhang, F. Yang, and X. Wang. The recent progress of mems/nems resonators. *Micromachines*, 12(6), 2021.

[59] S. Schmid, L. G. Villanueva, and M. L. Roukes. *Fundamentals of Nanomechanical Resonators*. Springer Cham, 2 edition, 2023. 1 b/w illustrations, eBook published 18 May 2023.

[60] K. L. Ekinci and M. L. Roukes. Nanoelectromechanical systems. *Review of Scientific Instruments*, 76(6):061101, 05 2005.

[61] Mingwei Li, Rustom B. Bhiladvala, Thomas J. Morrow, James A. Sioss, Kok-Keong Lew, Joan M. Redwing, Christine D. Keating, and Theresa S. Mayer. Bottom-up assembly of large-area nanowire resonator arrays. *Nature Nanotechnology*, 3(2):88–92, 2008.

[62] S. Yadav, S. Tripathy, and D. Sarkar. Nems sensors based on novel nanomaterials. In Z. Yang, editor, *Advanced MEMS/NEMS Fabrication and Sensors*, page Chapter 6. Springer, 2022.

[63] D. A. Russell. Vibrational modes of a square membrane, 2002. Retrieved from https://www.acs.psu.edu/drussell/demos/membranesquare/square.html.

[64] M.-H. Chien. *Nanoelectromechanical photothermal microscopy and spectroscopy for single-molecule detection and imaging at room temperature*. Dissertation, Technische Universität Wien, 2021. Published on repositUm.

[65] A. Bouchaala, A. H. Nayfeh, and M. I. Younis. Analytical study of the frequency shifts of micro and nano clamped–clamped beam resonators due to an added mass. *Meccanica*, 52:333–348, 2017.

[66] A. N. Cleland and M. L. Roukes. Fabrication of high frequency nanometer scale mechanical resonators from bulk si crystals. *Applied Physics Letters*, 69(18):2653–2655, 1996.

[67] A. N. Cleland and M. L. Roukes. External control of dissipation in a nanometer-scale radiofrequency mechanical resonator. *Sensors and Actuators A: Physical*, 72(3):256–261, 1999.

[68] K. C. Schwab. Spring constant and damping constant tuning of nanomechanical resonators using a single-electron transistor. *Applied Physics Letters*, 80(7):1276–1278, 2002.

[69] Silvan Schmid, T. Bagci, E. Zeuthen, J. M. Taylor, P. K. Herring, M. C. Cassidy, C. M. Marcus, L. Guillermo Villanueva, B. Amato, A. Boisen, Y. Cheol Shin, J. Kong, A. S. Sørensen, K. Usami, and E. S. Polzik. Single-layer graphene on silicon nitride micromembrane resonators. *Journal of Applied Physics*, 115(5):054513, 2014.

[70] X. Yu, J. Thaysen, O. Hansen, and A. Boisen. Optimization of sensitivity and noise in piezoresistive cantilevers. *Journal of Applied Physics*, 92(10):6296–6301, 2002.

[71] A. Boisen, J. Thaysen, H. Jensenius, and O. Hansen. Environmental sensors based on micromachined cantilevers with integrated read-out. *Ultramicroscopy*, 82(1-4):11–16, 2000.

[72] M. Li, H. X. Tang, and M. L. Roukes. Ultra-sensitive nems-based cantilevers for sensing, scanned probe and very high-frequency applications. *Nature Nanotechnology*, 2(2):114–120, 2007.

[73] R. B. Karabalin, M. H. Matheny, X. L. Feng, E. Defay, G. Le Rhun, C. Marcoux, S. Hentz, P. Andreucci, and M. L. Roukes. Piezoelectric nanoelectromechanical resonators based on aluminum nitride thin films. *Applied Physics Letters*, 95(10):103111, 2009.

[74] N. Sinha, G. E. Wabiszewski, R. Mahameed, V. V. Felmetsger, S. M. Tanner, R. W. Carpick, and G. Piazza. Piezoelectric aluminum nitride nanoelectromechanical actuators. *Applied Physics Letters*, 95(5):053106, 2009.

[75] A. Barg, Y. Tsaturyan, E. Belhage, W. H. P. Nielsen, C. B. Møller, and A. Schliesser. Measuring and imaging nanomechanical motion with laser light. *Applied Physics B*, 123(1):8, 2017.

[76] G. Anetsberger, O. Arcizet, E. Gavartin, Q. P. Unterreithmeier, E. M. Weig, J. P. Kotthaus, and T. J. Kippenberg. Near-field cavity optomechanics with nanomechanical oscillators. In *Conference on Lasers and Electro-Optics (CLEO) and Quantum Electronics and Laser Science Conference (QELS)*. IEEE, 2010.

[77] S. Gröblacher, K. Hammerer, M. R. Vanner, and M. Aspelmeyer. Observation of strong coupling between a micromechanical resonator and an optical cavity field. *Nature*, 460(7256):724–727, 2009.

[78] H. Bešić, A. Demir, J. Steurer, N. Luhmann, and S. Schmid. Schemes for tracking resonance frequency for micro- and nanomechanical resonators. *Physical Review Applied*, 20(2):024023, 2023.

[79] A. Demir. Understanding fundamental trade-offs in nanomechanical resonant sensors. *Journal of Applied Physics*, 129:044503, 2021.

[80] P. Sadeghi, A. Demir, L. G. Villanueva, H. Kähler, and S. Schmid. Frequency fluctuations in nanomechanical silicon nitride string resonators. *Physical Review B*, 102(21):214106, 2020.

[81] Markus Piller, Pedram Sadeghi, Robert G. West, Niklas Luhmann, Paolo Martini, Ole Hansen, and Silvan Schmid. Thermal radiation dominated heat transfer in nanomechanical silicon nitride drum resonators. *Applied Physics Letters*, 117(3):034101, 07 2020.

[82] Maksymilian Kurek, Matthias Carnoy, Peter E. Larsen, Line H. Nielsen, Ole Hansen, Thomas Rades, Silvan Schmid, and Anja Boisen. Nanomechanical infrared spectroscopy with vibrating filters for pharmaceutical analysis. *Angewandte Chemie International Edition*, 56(14):3901–3905, 2017.

[83] Silvan Schmid, Maksymilian Kurek, Jens Q. Adolphsen, and Anja Boisen. Real-time single airborne nanoparticle detection with nanomechanical resonant filter-fiber. *Scientific Reports*, 3(1):1288, 2013.

[84] H. Bešić, A. Demir, V. Vukićević, J. Steurer, and S. Schmid. Adaptable frequency counter with phase filtering for resonance frequency monitoring in nanomechanical sensing. *IEEE Sensors Journal*, 2024. Accepted for publication.

[85] S. Yamada, S. Schmid, T. Larsen, O. Hansen, and A. Boisen. Photothermal infrared spectroscopy of airborne samples with mechanical string resonators. *Analytical Chemistry*, 85(21):10531–10535, 2013. PMID: 24083320.

[86] H. Bešić, A. Deutschmann-Olek, K. Mešić, K. Kanellopulos, and S. Schmid. Optimized signal estimation in nanomechanical photothermal sensing via thermal response modeling and kalman filtering. *IEEE Sensors Journal*, 24(19):30264–30274, 2024.

[87] F. Samaeifar, A. C. Ceccacci, S. B. Goswami, L. H. Nielsen, A. Afifi, K. Zór, and A. Boisen. Evaluation of the solid state form of tadalafil in sub-micron thin films using nanomechanical infrared spectroscopy. *International Journal of Pharmaceutics*, 565:227–232, 2019.

[88] A. Casci Ceccacci, A. Cagliani, P. Marizza, S. Schmid, and A. Boisen. Thin film analysis by nanomechanical infrared spectroscopy. *ACS Omega*, 4(4):7628–7635, 2019.

[89] T. Biswas, N. Miriyala, C. Doolin, X. Liu, T. Thundat, and J. Davis. Femtogram-scale photothermal spectroscopy of explosive molecules on nanostrings. *Analytical Chemistry*, 86(22):11368–11372, 2014.

[90] Jelena Timarac-Popović, Johannes Hiesberger, Eldira Šesto, Niklas Luhmann, Ariane Giesriegl, Hajrudin Bešić, Josiane P. Lafleur, and Silvan Schmid. Nanoplastic analysis with nanoelectromechanical system fourier transform infrared spectroscopy: Nems–ftir. *Unpublished manuscript*, 2025. Manuscript in preparation.

[91] Martin G. J. Löder, Marianna Kuczera, Sigrid Mintenig, Claudia Lorenz, and Gunnar Gerdts. Focal plane array detector-based micro-fourier-transform infrared imaging for the analysis of microplastics in environmental samples. *Environmental Chemistry*, 12(5):563–581, 2015.

[92] Jessica Caldwell, Patricia Taladriz-Blanco, Roman Lehner, Andriy Lubskyy, Roberto Diego Ortuso, Barbara Rothen-Rutishauser, and Alke Petri-Fink. The micro-, submicron-, and nanoplastic hunt: A review of detection methods for plastic particles. *Chemosphere*, 293:133514, 2022.

[93] Alexander S. Tagg, Melanie Sapp, Jesse P. Harrison, and Jesús J. Ojeda. Identification and quantification of microplastics in wastewater using focal plane array-based reflectance micro-ft-ir imaging. *Analytical Chemistry*, 87(12):6032–6040, 2015. PMID: 25986938.

[94] William C Hinds and Yifang Zhu. *Aerosol technology: properties, behavior, and measurement of airborne particles*. John Wiley & Sons, 2022.

[95] Chiara Leuschner. Design and characterisation of an aerosol sampling chamber for mobile sampling of airborne particles. Bachelor's thesis, Institute of Sensors and Actuator Systems, TU Wien, 2022.

[96] Silvan Schmid, Maksymilian Kurek, Jens Q Adolphsen, and Anja Boisen. Real-time single airborne nanoparticle detection with nanomechanical resonant filter-fiber. *Scientific reports*, 3(1):1288, 2013.

[97] Invisible Light Labs. Emilie sampler. https://invisible-light-labs.com/our-products/emilie-sampler/, n.d. Accessed: 2025-05-21.

[98] M. Piller, J. Hiesberger, E. Wistrela, P. Martini, N. Luhmann, and S. Schmid. Thermal ir detection with nanoelectromechanical silicon nitride trampoline resonators. *IEEE Sensors Journal*, 23(2):1066–1071, 2022.

[99] Mária Porubská, Ondrej Szöllös, Alena Kóňová, Ivica Janigová, Miloslava Jašsková, Klaudia Jomová, and Ivan Chodák. Ftir spectroscopy study of polyamide-6 irradiated by electron and proton beams. *Polymer Degradation and Stability*, 97(4):523–531, 2012.

[100] N. Vasanthan and D. R. Salem. Ftir spectroscopic characterization of structural changes in polyamide-6 fibers during annealing and drawing. *Journal of Polymer Science Part B: Polymer Physics*, 39(5):536–547, 2001.

[101] Xinshu Li, Qing Wang, Dongyang Wu, Tingqu Li, Peng Zhang, Jingru Bai, and Xu Zhang. Effects of short-term thermal oxidation on the mechanical and thermal behavior of pa6 liner material for type iv hydrogen storage cylinders. *RSC Advances*, 15(21):16375–16391, 2025.

[102] Brian C. Smith. Infrared spectroscopy of polymers, xi: Introduction to organic nitrogen polymers. *Spectroscopy*, 38(03):14–18, 2023.

[103] Kaihua Shi, Lin Ye, and Guangxian Li. Thermal oxidative aging behavior and stabilizing mechanism of highly oriented polyamide 6. *Journal of Thermal Analysis and Calorimetry*, 126, 05 2016.

[104] Larissa Stieven Montagna, Guilherme Ferreira de Melo Morgado, Juliano Marini, Thaís Larissa do Amaral Montanheiro, Alessandro Guimarães, Fabio Roberto Passador, and Mirabel Cerqueira Rezende. Effect of accelerated weathering environment on the carbon fiber/polyamide 6 composites. *Polímeros: Ciência e Tecnologia*, 33(3):e20230032, 2023.

[105] Ke Liu, Yuanyuan Li, Lei Tao, and Ru Xiao. Preparation and characterization of polyamide 6 fibre based on a phosphorus-containing flame retardant. *RSC Advances*, 8(17):9261–9271, 2018.

[106] C. Campanale, I. Savino, C. Massarelli, and V. F. Uricchio. Ftir spectroscopy to assess the degree of alteration of artificially aged and environmentally weathered microplastics. *Polymers*, 15(911), 2023.

[107] T. Borgmeyer, L. Zhou, F. Breider, M. J. Rossi, and C. Ludwig. Natural and simulated weathering of polystyrene: A molecular view of the polymeric interface. *Science of The Total Environment*, 947:174609, 2024.

[108] B. C. Smith. The infrared spectra of polymers iii: Hydrocarbon polymers. *Spectroscopy*, 36(11):22–25, 2021.

[109] Brian C. Smith. Infrared spectral interpretation, in the beginning i: The meaning of peak positions, heights, and widths. *Spectroscopy*, 39(04):18–24, May 2024.

[110] L. M. Hernandez, E. G. Xu, H. C. E. Larsson, R. Tahara, V. B. Maisuria, and N. Tufenkji. Plastic teabags release billions of microparticles and nanoparticles into tea. *Environmental Science Technology*, 53(21):12300–12310, 2019.

[111] G. Banaei, D. Abass, A. Tavakolpournegari, J. Martín-Pérez, J. Gutiérrez, G. Peng, T. Reemtsma, R. Marcos, A. Hernández, and A. García-Rodríguez. Teabag-derived micro/nanoplastics (true-to-life mnpls) as a surrogate for real-life exposure scenarios. *Chemosphere*, 368:143736, 2024.